Atmospheric
Measurement
Techniques

Accomplishments of the MUSICA project to provide accurate, long-term, global and high-resolution observations of tropospheric {H₂O,δD} pairs – a review

Matthias Schneider[1], Andreas Wiegele[1], Sabine Barthlott[1], Yenny González[2,3,a], Emanuel Christner[1], Christoph Dyroff[1,b], Omaira E. García[2], Frank Hase[1], Thomas Blumenstock[1], Eliezer Sepúlveda[2], Gizaw Mengistu Tsidu[4,5], Samuel Takele Kenea[4,c], Sergio Rodríguez[2], and Javier Andrey[6,d]

[1]Institute of Meteorology and Climate Research (IMK-ASF), Karlsruhe Institute of Technology, Karlsruhe, Germany
[2]Izaña Atmospheric Research Center, Agencia Estatal de Meteorología (AEMET), Santa Cruz de Tenerife, Spain
[3]Sieltec Canarias, S.L., Hábitat 2, 38204, San Cristóbal de La Laguna, Santa Cruz de Tenerife, Spain
[4]Department of Physics, Addis Ababa University, P.O. Box 1176, Addis Ababa, Ethiopia
[5]Botswana International University of Technology and Science (BIUST) Priv. Bag 16, Palapye, Botswana
[6]Area de Investigación e Instrumentación Atmosférica, INTA, Torrejón de Ardoz, Spain
[a]now at: Dept. of Earth, Atmospheric, and Planetary Sciences, Massachusetts Institute of Technology, 77 Massachusetts Avenue, Cambridge, MA 02139-4307, USA
[b]now at: Aerodyne Research Inc., 45 Manning Road, Billerica, MA 01821, USA
[c]now at: Department of Physics, Samara University, P.O. Box 132, Samara, Ethiopia
[d]now at: CNRM-GAME, Météo France and CNRS, Toulouse, France

Correspondence to: Matthias Schneider (matthias.schneider@kit.edu)

Abstract. In the lower/middle troposphere, {H₂O,δD} pairs are good proxies for moisture pathways; however, their observation, in particular when using remote sensing techniques, is challenging. The project MUSICA (MUlti-platform remote Sensing of Isotopologues for investigating the Cycle of Atmospheric water) addresses this challenge by integrating the remote sensing with in situ measurement techniques. The aim is to retrieve calibrated tropospheric {H₂O,δD} pairs from the middle infrared spectra measured from ground by FTIR (Fourier transform infrared) spectrometers of the NDACC (Network for the Detection of Atmospheric Composition Change) and the thermal nadir spectra measured by IASI (Infrared Atmospheric Sounding Interferometer) aboard the MetOp satellites. In this paper, we present the final MUSICA products, and discuss the characteristics and potential of the NDACC/FTIR and MetOp/IASI {H₂O,δD} data pairs.

First, we briefly resume the particularities of an {H₂O,δD} pair retrieval. Second, we show that the remote sensing data of the final product version are absolutely calibrated with respect to H₂O and δD in situ profile references measured in the subtropics, between 0 and 7 km. Third, we reveal that the {H₂O,δD} pair distributions obtained from the different remote sensors are consistent and allow distinct lower/middle tropospheric moisture pathways to be identified in agreement with multi-year in situ references. Fourth, we document the possibilities of the NDACC/FTIR instruments for climatological studies (due to long-term monitoring) and of the MetOp/IASI sensors for observing diurnal signals on a quasi-global scale and with high horizontal resolution. Fifth, we discuss the risk of misinterpreting {H₂O,δD} pair distributions due to incomplete processing of the remote sensing products.

1 Introduction

Atmospheric moisture (condensed water and vapour) strongly interacts with solar as well as thermal radiances and distributes energy in the form of latent heat. In consequence, it has a wide impact on the atmospheric energy budget and strongly affects circulation on regional and global scales. The insufficient understanding of tropospheric moisture pathways and their coupling to atmospheric circulation is seen as a major challenge for climate system modelling (e.g. Stevens and Bony, 2013), and a focus on three specific research areas is recommended (http://www.wcrp-climate.org/grand-challenges): first, the low cloud feedback and the responsible physical processes (modelled equilibrium climate sensitivity is strongly linked to the low cloud feedback, e.g. Sherwood et al., 2014); second, the climate response of large-scale tropospheric circulation systems and precipitation patterns (whereby palaeoclimate archives offer valuable possibilities, e.g. Ortega et al., 2015); third, the coupling between small-scale processes and large-scale dynamics (e.g. cloud processes that take place on diurnal timescale can significantly affect large-scale circulation, Marsham et al., 2013).

Simultaneous observations of different tropospheric water isotopologues can aid advancements in these research areas. The ratio between the different water isotopologues provides information on processes related to moisture uptake, exchange, clouds and atmospheric transportation upwind of the detected air mass (e.g. Dansgaard, 1964; Gat, 2000; Yoshimura et al., 2004), thereby offering potential for investigating the coupling between atmospheric circulation and moisture pathways.

Furthermore, the water isotopologue ratios archived in ice cores, speleothems, lake sediments or tree rings contain information about past climate conditions (e.g. Ortega et al., 2015), whose reconstruction, however, relies on a comprehensive understanding of the linkages between the archived isotopologues, on the one hand, and the tropospheric isotopologues, temperature and circulation, on the other hand.

The isotopologue ratios are typically expressed in the δ notation, which relates the observed ratio to the standard ratio VSMOW (Vienna Standard Mean Ocean Water). For instance, the HDO / H₂O ratio is typically expressed as $\delta D = \frac{HDO/H_2O}{VSMOW} - 1$. Here and in the following we use H₂O and HDO as equivalent to $H_2^{16}O$ and $HD^{16}O$, respectively. The consideration of other isotopologues will be specified explicitly (e.g $H_2^{18}O$ or $H_2^{17}O$).

During the last years there has been great progress in observations of the tropospheric water vapour isotopologues, whereby remote sensing observations are particularly interesting since they can be performed continuously (for cloud-free conditions). Ground-based remote sensing can offer long-term data records. There are the ground-based water vapour isotopologue remote sensing retrievals using the NDACC (Network for the Detection of Atmospheric Com-

position Change) middle infrared spectra (Schneider et al., 2012, and references therein) and retrievals that use the TCCON (Total Carbon Column Observing Network) near-infrared spectra (e.g. Rokotyan et al., 2014). Tropospheric water vapour isotopologue data sets have also been presented using space-based sensors. There are different research groups using short-wave infrared (SWIR) spectra measured by the satellite sensors SCIAMACHY (Frankenberg et al., 2009; Scheepmaker et al., 2015) or GOSAT (Boesch et al., 2013; Frankenberg et al., 2013) as well as the thermal nadir spectra of TES (Thermal Emission Spectrometer; Worden et al., 2006, 2012) or IASI (Infrared Atmospheric Sounding Interferometer; Schneider and Hase, 2011; Lacour et al., 2012; Wiegele et al., 2014).

While in the dry upper troposphere and stratosphere δD observations alone allow significant conclusions on the moisture pathways from the troposphere to the stratosphere and on stratospheric circulation (e.g. Kuang et al., 2003; Steinwagner et al., 2010), the situation is different in the lower and middle troposphere. There, humidity is much more variable and the moisture pathways can be best investigated by analysing the distribution of the {H₂O,δD} pairs (e.g. Galewsky et al., 2005; Noone, 2012; González et al., 2016). Recently, there have been a variety of publications that use remote sensing observations of tropospheric {H₂O,δD} pairs for tropospheric moisture pathway studies: for instance, for estimating the importance of rain recycling (e.g. Worden et al., 2007), for investigating the dynamics of the Madden-Julian oscillation (e.g. Berkelhammer et al., 2012; Tuinenburg et al., 2015) or for drawing conclusions on vertical mixing processes (e.g. Noone, 2012; Risi et al., 2012a; Sutanto et al., 2015). However, there are very few studies so far where attempts have been made to empirically validate these {H₂O,δD} pairs (Schneider et al., 2015; Lacour et al., 2015). Further and more detailed validation efforts for the {H₂O,δD} pairs are urgently needed because an estimation of {H₂O,δD} pairs is complex and not the same as an individual optimal estimation of H₂O and HDO (nor of H₂O and δD). The reason is that the sensitivities for H₂O and HDO (and also for H₂O and δD) are generally different (Schneider et al., 2006; Worden et al., 2006; Schneider et al., 2012).

A further pending detail with the isotopologue remote sensing data is the unclear bias in δD, which can significantly compromise their scientific usefulness (e.g. Risi et al., 2012b; Field et al., 2014; Yoshimura et al., 2014). First empirical bias assessment studies were presented by Schneider and Hase (2011) and Worden et al. (2011). For a reliable bias documentation, we need vertical isotopologue reference profiles measured by well-calibrated in situ instrumentation (Herman et al., 2014; Dyroff et al., 2015). Currently we are only aware of one campaign (the summer 2013 MUSICA (MUlti-platform remote Sensing of Isotopologues for investigating the Cycle of Atmospheric water) campaign, Dyroff et al., 2015), where such profiles are measured in coincidence with ground- and space-based remote sensing observations

and over the wide altitude range where the remote sensors are sensitive.

Removing the shortcomings in tropospheric water vapour isotopologue remote sensing data has been a focus of the project MUSICA (http://www.imk-asf.kit.edu/english/musica.php). In this paper, we summarize the final results of the MUSICA project, whose most relevant papers are collected in Appendix A. We demonstrate that calibrated, long-term, global and high-resolution remote sensing data of tropospheric {$H_2O,\delta D$} pairs can be produced. In Sect. 2, we give a brief review on the theory of {$H_2O,\delta D$} pair estimations and of the MUSICA NDACC/FTIR (Fourier transform infrared) and MetOp/IASI retrievals, in particular. Section 3 documents that the final MUSICA data are well-calibrated with respect to in situ H_2O and δD references. Section 4 shows an empirical validation of the {$H_2O,\delta D$} pair distributions by intercomparing the {$H_2O,\delta D$} signals observed by in situ instruments, NDACC/FTIR, MetOp/IASI-A and MetOp/IASI-B for different atmospheric situations. Sections 5 and 6 document the possibilities offered by the unique long-term characteristics of the NDACC/FTIR data and by the unique spatial and temporal coverage of the MetOp/IASI observations. In Sect. 7 we discuss risks for defective interpretations of the {$H_2O,\delta D$} remote sensing data pairs. Section 8 gives a summary.

2 Remote sensing of water vapour isotopologues and their ratios

In this section, we give a very brief overview on the challenges of tropospheric water vapour isotopologue remote sensing. Then we resume the retrieval approaches as developed in preparation for and continuously improved during the project MUSICA. In addition to the MUSICA products, there are other ground- and space-based (non-MUSICA) tropospheric water vapour isotopologue remote sensing products. A brief overview and a short discussion of the differences to the MUSICA products is given in Appendix B.

2.1 The challenge

In situ instruments analyse a clearly defined air mass and from the H_2O and HDO measurements the ratio (δD) can be directly calculated. This is more complicated for remote sensing observations. There, the amount of H_2O and HDO along the line of sight is retrieved from the measured spectra. The sensitivity of the retrieval depends on the noise in the spectra and on the shape and strength of the different spectral lines. Typically, the sensitivity for H_2O is different to the sensitivity for HDO and the retrieved H_2O value represents a different altitude range than the retrieved HDO value (H_2O and HDO have different averaging kernels). In consequence, the δD values calculated from individual H_2O and

HDO retrievals can be rather misleading. Instead of individual retrievals, a combined H_2O and HDO retrieval is needed.

A logarithmic-scale retrieval of H_2O and HDO together with a constraint of $\ln[HDO] - \ln[H_2O]$ has been proposed by Schneider et al. (2006) and Worden et al. (2006) for generating δD values by remote sensing techniques. This approach means actually an optimal estimation of $(\ln[H_2O] + \ln[HDO])/2$ and $\ln[HDO] - \ln[H_2O]$, which are good proxies for H_2O and δD (Schneider et al., 2012); i.e. it is a quasi-optimal estimation of H_2O and δD. However, it is an individual optimal estimation of H_2O and δD, and thus such a product is still not comparable to the {$H_2O,\delta D$} pairs obtained from the in situ measurements. The reason is that the remote sensing system is more sensitive to atmospheric H_2O than to atmospheric δD and in addition there is a slight cross-dependency of the retrieved δD on atmospheric H_2O (e.g. Schneider et al., 2012).

2.2 The MUSICA {$H_2O,\delta D$} pair product

The aforementioned problems can be overcome by an a posteriori processing of the retrieval output. The result of the a posteriori processing is an estimation of {$H_2O,\delta D$} pairs that are comparable to the {$H_2O,\delta D$} pairs obtained from in situ measurements. In the following, we give a very brief explanation of the necessity and functionality of the a posteriori processing.

The remote sensing retrievals produce state vectors $\boldsymbol{x}$, averaging kernels $\mathbf{A}$, error covariance matrices $\mathbf{S}$, etc., for the {$\ln[H_2O], \ln[HDO]$} basis system (or for the {$\ln[H_2^{16}O], \ln[H_2^{18}O], \ln[HD^{16}O]$} basis system, if isotopologues with different oxygen atoms are distinguished). However, besides H_2O (99.7 % in form of $H_2^{16}O$), we are actually interested in δD, and eventually deuterium excess (d $= \delta D - 8\delta^{18}$, with $\delta^{18} = \frac{H_2^{18}O/H_2^{16}O}{VSMOW} - 1$). These parameters, their variations and uncertainties can be captured and characterized in an elegant manner by using the {$H_2O,\delta D$} (or {$H_2O,\delta D,d$}) proxy basis system: the basis {$(\ln[H_2O] + \ln[HDO])/2$} (or {$(\ln[H_2^{16}O] + \ln[H_2^{18}O] + \ln[HD^{16}O])/3$}, if we distinguish between the isotopologues with different oxygen atoms) well captures the parallel variations of the different isotopologues and is thus a good proxy for the dominant H_2O variations. Variations in δD are 1 order of magnitude smaller, for which the basis {$\ln[HDO] - \ln[H_2O]$} (or {$\ln[HD^{16}O] - \ln[H_2^{16}O]$}) is a good proxy. Variations in deuterium excess are a further order of magnitude smaller, for which we can use the proxy basis {$7\ln[H_2^{16}O] - 8\ln[H_2^{18}O] + \ln[HD^{16}O]$} (Barthlott et al., 2016a).

The transformation of this proxy basis system can easily be realized by a transformation operator $\mathbf{P}$, and the transformed state vector, averaging kernel and any covariance matrix ($\boldsymbol{x'}$, $\mathbf{A'}$ and $\mathbf{S'}$) are then given by

$$x' = \mathbf{P}x$$
$$\mathbf{A}' = \mathbf{P}\mathbf{A}\mathbf{P}^{-1}$$
$$\mathbf{S}' = \mathbf{P}\mathbf{S}\mathbf{P}^T. \tag{1}$$

In the proxy basis system, the different sensitivities with respect to H_2O and δD and the cross-dependencies become clearly visible. We can remove these deficits by the a posteriori processing, which consists of simple matrix multiplications (using the a posteriori correction operator $\mathbf{C}$). The a posteriori corrected state vector, averaging kernel and any covariance matrix (x^*, $\mathbf{A}^*$ and $\mathbf{S}^*$) can be calculated as

$$x^* = \mathbf{C}(x' - x'_a) + x'_a$$
$$\mathbf{A}^* = \mathbf{C}\mathbf{A}'$$
$$\mathbf{S}^* = \mathbf{C}\mathbf{S}'\mathbf{C}^T. \tag{2}$$

In the MUSICA papers, this a posteriori processed product is also often called the Type 2 product, and since it is most useful for isotopologue studies (H_2O and δD have almost the same averaging kernels), it will be the product that is generally used in this work. In addition, MUSICA offers a Type 1 product which is not a posteriori processed and it is the kind of product that is generally distributed by other data producers. It consists of optimal H_2O data, but has limited possibilities for isotopologue studies (see discussion in Sect. 7).

Readers that are interested in more details about the proxy state method, the a posteriori correction and the operators $\mathbf{P}$ and $\mathbf{C}$ as used in Eqs. (1) and (2) are recommended to study Schneider et al. (2012), Wiegele et al. (2014) and Barthlott et al. (2016a). However, we would like to note that the MU-SICA remote sensing data users do not have to be concerned about details of the a posteriori processing. The processing does not have to be performed by the data users because the data are provided as an a posteriori processed product (Type 2) and also in the form of the direct retrieval output (H_2O and HDO or H_2O and δD products that have not been a posteriori processed, Type 1 product).

2.3 The MUSICA ground-based products

The MUSICA ground-based remote sensing retrieval uses the PROFFIT retrieval code (Hase et al., 2004) and the middle-infrared spectra recorded within the NDACC (www. acom.ucar.edu/irwg/). The NDACC spectra are of very high spectral resolution (0.005 cm^{-1}) and offer $H_2^{16}O$, $H_2^{18}O$ and $HD^{16}O$ absorption lines of similar strength.

For the final MUSICA retrieval version (v2015), we perform an optimal estimation of $(\ln[H_2^{16}O] + \ln[H_2^{18}O] + \ln[HD^{16}O])/3$, $\ln[HD^{16}O] - \ln[H_2^{16}O]$ and $7\ln[H_2^{16}O] - 8\ln[H_2^{18}O] + \ln[HD^{16}]$, which are good proxies for H_2O, δD and d (deuterium excess). In addition to the cross-constrained

fit of the water vapour isotopologues $H_2^{16}O$, $H_2^{18}O$ and $HD^{16}O$, we perform simultaneous but individual fits (no cross-constraints) for profiles of the water vapour isotopologue $H_2^{17}O$, the temperature and the interfering species CO_2, O_3, N_2O, CH_4 and HCl. The code PROFFIT uses the root mean square value of the residual (difference between simulated and measured radiances) as noise level for constraining the retrievals. We use HITRAN 2012 parameters (Rothman et al., 2013) optimized for speed-dependent Voigt line parameterization. Details on the general retrieval set-up are given in Schneider et al. (2012) and the modifications made for v2015 are summarized in Barthlott et al. (2016a).

The Type 1 MUSICA NDACC/FTIR product provides water vapour profiles for the lower, middle and upper troposphere (DOFS, degree of freedom of signal, of almost 3). The Type 2 product (the a posteriori corrected product) offers consistent {H_2O,δD} pairs, which are sensitive to the lower and the middle troposphere, whereby it is possible to reasonably separate both altitude regions (DOFS of about 1.7). This is illustrated in Fig. 1, which shows the rows of the averaging kernel matrix ($\mathbf{A}^*$) in the {H_2O,δD,d} proxy basis system and after applying the a posteriori correction (see Eq. 2). The full averaging kernels matrix consists of nine blocks, each of which is a {nol × nol} matrix, whereby {nol} is the number of the vertical atmospheric grid points used for the retrieval. In total, $\mathbf{A}^*$ has the dimension {(nol × 3) × (nol × 3)}:

$$\mathbf{A}^* = \begin{pmatrix} \mathbf{A}^*_{11} & \mathbf{A}^*_{12} & \mathbf{A}^*_{13} \\ \mathbf{A}^*_{21} & \mathbf{A}^*_{22} & \mathbf{A}^*_{23} \\ \mathbf{A}^*_{31} & \mathbf{A}^*_{32} & \mathbf{A}^*_{33} \end{pmatrix}. \tag{3}$$

The three blocks along the diagonal describe the direct responses; i.e. they represent the averaging kernels for the H_2O, δD and d proxies. Figure 1 demonstrates that the sensitivity with respect to H_2O and δD is very similar (compare plots showing the entries of $\mathbf{A}^*_{11}$ and $\mathbf{A}^*_{22}$), which is achieved by the a posteriori processing. The outer diagonal blocks describe the cross-responses, whereby in Fig. 1 the respective x axes are scaled, thereby accounting for the different magnitudes of the H_2O, δD and d variations. Concerning the cross-responses between H_2O and δD, we have to consider that $\ln[H_2O]$ variations are 1 order of magnitude larger than δD variations. This means that the entries in the $\mathbf{A}^*_{12}$ block must be 10 times larger than entries in the $\mathbf{A}^*_{11}$ block in order to be of similar importance. Vice versa, entries in the $\mathbf{A}^*_{21}$ block can be 1 order of magnitude smaller than entries in the $\mathbf{A}^*_{22}$ block and still have a similar importance. The blocks $\mathbf{A}^*_{31}$, $\mathbf{A}^*_{32}$ and $\mathbf{A}^*_{33}$ describe how the retrieved d proxy responds to real atmospheric variations. Although there is sensitivity with respect to real atmospheric deuterium excess (see entries of $\mathbf{A}^*_{33}$), the retrieved d signals are mainly caused by variations in H_2O and δD (significant entries in blocks $\mathbf{A}^*_{31}$ and $\mathbf{A}^*_{32}$). The situation can be improved by an alternative a posteriori processing being dedicated to {H_2O,δD,d} triplets (see Sect. 4.4.2 in Barthlott et al., 2016a), which is, however,
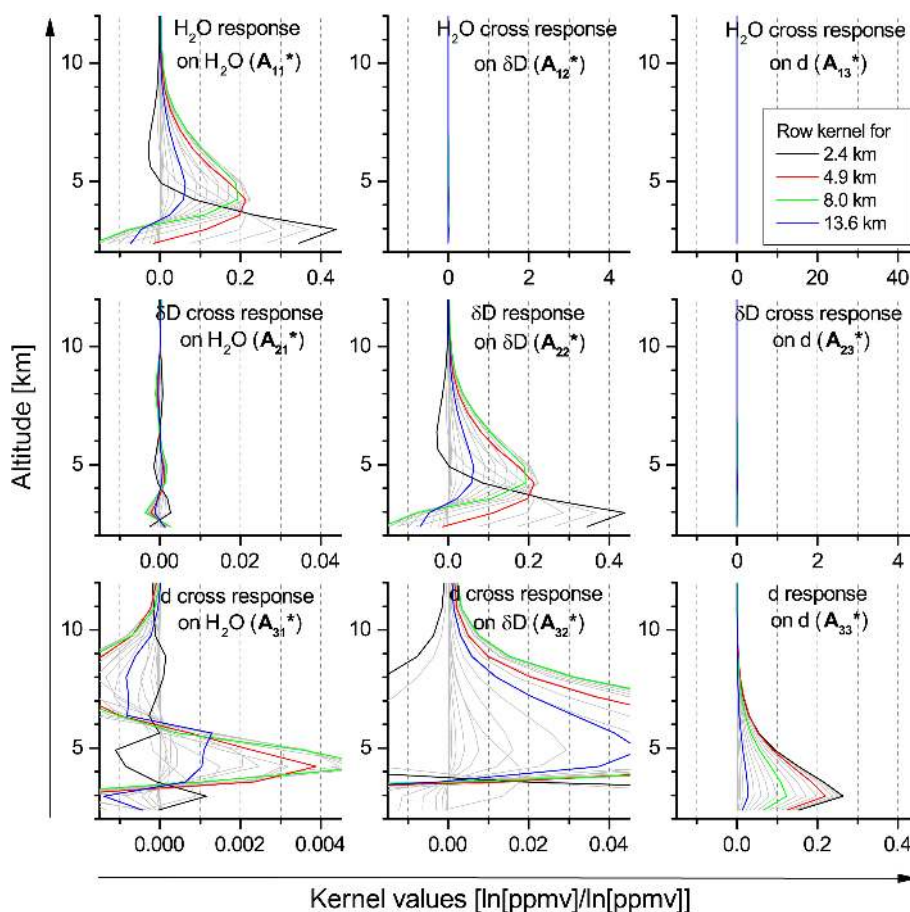
Figure 1. Row entries of the nine blocks of the NDACC/FTIR full averaging kernel matrix in the {H$_2$O,δD,d} proxy basis system and after a posteriori correction ($\mathbf{A}^*$ as given in Eq. 3). The kernel is for the retrieval of a ground-based FTIR spectrum measured on 09:41 UT on 24 Jul 2013 (the retrieval result of this measurement is one of the data points shown in Fig. 3).

not subject of this paper. For this paper and in order to understand the {H$_2$O,δD} pair signals, it is sufficient to work with the kernel blocks $\mathbf{A}^*_{11}$, $\mathbf{A}^*_{12}$, $\mathbf{A}^*_{21}$ and $\mathbf{A}^*_{22}$.

Error estimations are discussed in detail in Schneider et al. (2012). The random error is about 2 % for H$_2$O and 25‰ for δD, whereby the leading error source is uncertainty in the atmospheric temperature profiles and artefacts in the spectral baseline (like channelling or offset). Systematic errors are dominated by uncertainties in the spectroscopic parameters. Already for small uncertainties of 1 and 2 % for line intensity and pressure broadening parameters, the systematic errors in H$_2$O and δD "profiles" can reach 10 % and 150‰, respectively. An empirical study indicates that for the v2015 data, the bias is actually much smaller (see Sect. 3). In addition, for an atmosphere with fine vertical structures, the δD cross-dependency on H$_2$O can reach 15‰ (see Fig. 9 in Schneider et al., 2012).

2.4 The MUSICA space-based products

For the MUSICA MetOp/IASI retrievals, a nadir version of PROFFIT is used. The basic retrieval set-up is presented and analysed in detail in Schneider and Hase (2011) and Wiegele et al. (2014). It has been developed in consistency with the NDACC/FTIR retrieval. It uses a broad spectral window (1190–1400 cm^{-1}), and performs an optimal estimation of the humidity and δD proxies ((ln[H$_2$O]+ln[HDO])/2 and ln[HDO] − ln[H$_2$O]). Simultaneously, we retrieve surface skin temperature and atmospheric temperature, as well as the interfering species CH$_4$, N$_2$O, CO$_2$ and HNO$_3$. Our MetOp/IASI retrieval does not distinguish between H$_2^{16}$O and H$_2^{18}$O because the spectroscopic signatures of the latter are very weak in the IASI spectra. So, we treat all water molecules with two hydrogen atoms as a single molecule (in the following referred to as H$_2$O), whose variability is mainly the one of H$_2^{16}$O. For our atmospheric temperature fit, we constrain strongly towards the EUMETSAT L2 atmospheric temperature. The root mean square value of the residual (dif-

ference between simulated and measured radiances) is used as noise level for constraining the retrievals.

The previous version of the MUSICA MetOp/IASI retrieval (Schneider and Hase, 2011; Wiegele et al., 2014) worked with HITRAN 2008 spectroscopic water vapour line parameters (Rothman et al., 2009). For the final MUSICA retrieval version (v2015) we use the HITRAN 2012 parameters (Rothman et al., 2013) and modified the line intensities (S) for the HDO absorption signatures by +10 %. We also tested modifications of S for the H$_2$O signatures and changes of γ_{air} (pressure broadening parameter), but finally found that a modification of S of HDO works most effectively for correcting biases in δD. In this context, we would like to remark that the bias correction as suggested for TES (Worden et al., 2011; Herman et al., 2014) is also consistent with a positive change of S of HDO.

The retrieval provides a Type 1 product of H$_2$O profiles that is sensitive to variations between the surface and about 15 km altitude (DOFS of about 4). The Type 2 product (consistent {H$_2$O,δD} pairs) has a typical DOFS of 0.7–1.0 (after filtering according to Sect. 6.2), whereby the sensitivity is mainly limited to the middle troposphere. This is illustrated in Fig. 2, which plots the rows of the averaging kernel matrix ($\mathbf{A}^*$) in the {H$_2$O,δD} proxy basis system and after applying the a posteriori correction. For the MetOp/IASI retrieval we have no deuterium excess basis and the dimension of $\mathbf{A}^*$ is $\{(nol \times 2) \times (nol \times 2)\}$

$$\mathbf{A}^* = \begin{pmatrix} \mathbf{A}_{11}^* & \mathbf{A}_{12}^* \\ \mathbf{A}_{21}^* & \mathbf{A}_{22}^* \end{pmatrix}. \tag{4}$$

As for the NDACC/FTIR kernels, $\mathbf{A}_{11}^*$ and $\mathbf{A}_{22}^*$ describe the sensitivities with respect to H$_2$O and δD, and $\mathbf{A}_{12}^*$ and $\mathbf{A}_{21}^*$ their cross-responses, respectively.

The random error is about 5 % for H$_2$O and 20 ‰ for δD, whereby atmospheric temperature uncertainties, thin elevated clouds and noise in the spectra are the leading uncertainty sources. The systematic error is dominated by uncertainties in the spectroscopic parameters. It can easily reach 5 % and 50 ‰ for H$_2$O and δD, respectively (in case of a 5 % uncertainty in the spectroscopic line intensity parameters). However, an empirical study as shown in Sect. 3 reveals that for v2015 the bias is actually much smaller. In addition, for an atmosphere with fine vertical structures, the δD cross-dependency on H$_2$O can occasionally be larger than 40 ‰ (see Fig. 5 in Wiegele et al., 2014).

2.5 Uniform a priori settings

For v2015, we work with the same globally constant water vapour isotopologue a priori data for all ground-based retrievals (different globally distributed NDACC/FTIR stations) and for all MetOp/IASI retrievals (for the whole globe). Thereby, we assure that observations at different locations are not affected by the use of different a priori data, and therefore an interpretation of regional differences (e.g. lati-
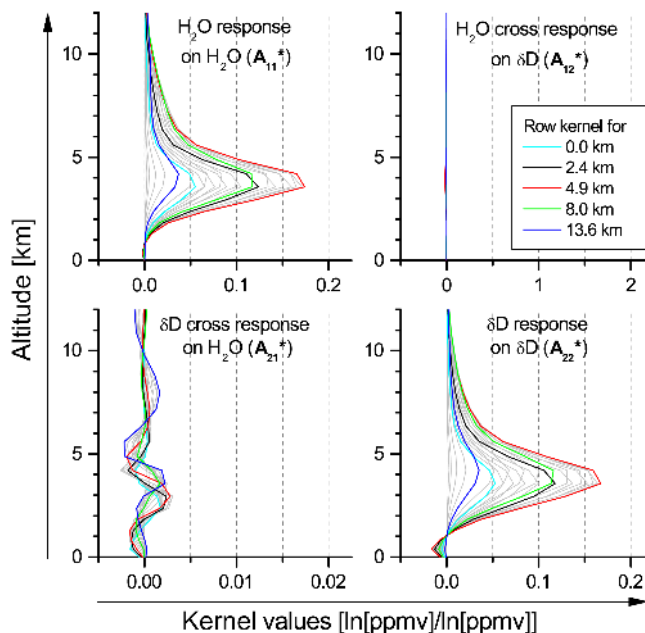

Figure 2. Row entries of the four blocks of the MetOp/IASI full averaging kernel matrix in the {H$_2$O,δD} proxy basis system and after a posteriori correction ($\mathbf{A}^*$ as given in Eq. 4). It is for a retrieval of an IASI spectrum measured on 11:07 UT on 24 Jul 2013 close to the southern coast of Tenerife (the retrieval result of this measurement is one of the data points shown in Fig. 4).

tudinal gradients) becomes rather straightforward. This is a further development of the previous retrieval version, where we used different a priori data for the (sub)tropics, the mid-latitudes and the polar regions.

The a priori profiles used are mean values of LMDZiso calculations (Risi et al., 2012b) and are as depicted in Fig. 2 of Lacour et al. (2012). As H$_2$O a priori variability, we assume 75 % in the boundary layer, 150 % in the middle and upper troposphere and 30 % in the stratosphere. For δD, the respective variability values are 60 ‰, 120 and 50 ‰. The a priori covariances are then calculated by assuming a correlation length of 2 km in the boundary layer, 4 km in the middle and upper troposphere and 8 km in the stratosphere.

3 Calibrated remote sensing products

The summer 2013 MUSICA campaign generated reliable H$_2$O and HDO (and δD) in situ reference profiles on 6 days between the sea surface and 6–7 km altitude (Dyroff et al., 2015; Schneider et al., 2015). From the δD profiles we calculate δ^{18} and then H$_2^{18}$O profiles by assuming δD = 8 × δ^{18} (H$_2^{18}$O is needed for validating the v2015 NDACC/FTIR product). The in situ profiles have been measured in coincidence with high-resolution ground-based FTIR observations and with IASI observations and are unique for documenting the bias in the remote sensing data because they cover the
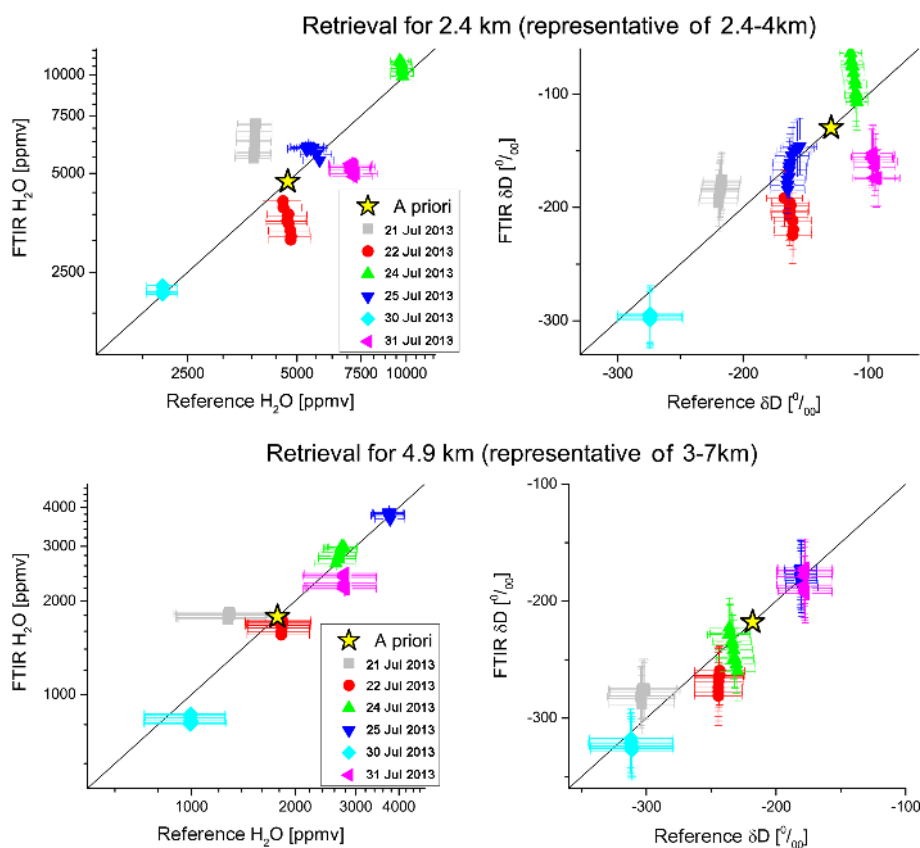
Figure 3. Correlation between the reference profiles (in situ data measured by the ISOWAT instrument for 0–7 km and climatology above, then smoothed with FTIR kernels) and FTIR data for FTIR measurements made in the morning (08:15–09:45 UT), i.e. before the aircraft flights, but reasonably representative of the free troposphere. Left panels are for H₂O and right panels are for δD. Upper panels for retrievals at 2.4 km and bottom panels for retrievals at 5 km. The black line is the 1 : 1 diagonal. The error bars represent the uncertainty estimations for the reference and FTIR data. Note that for the comparison at 5 km a large part of the uncertainty in the reference data is due to the fact that there are no ISOWAT measurements above the aircraft's ceiling altitude (Schneider et al., 2015, and discussion in Appendix C).

whole altitude range from the surface up to 6–7 km. In this section, we show that the MUSICA v2015 remote sensing products are well calibrated with respect to these reference data.

3.1 NDACC/FTIR

In a first study with data from the previous MUSICA NDACC/FTIR retrieval version, we found a bias of 25–70‰ for δD with respect to the profile references (see right panels in Figs. 9 and 10 of Schneider et al., 2015). That study was done with a limited data set (only one exemplary remote sensing observation per day). For the v2015 product we perform a comprehensive empirical bias assessment and compare the ground-based FTIR data obtained for all optimal coincidences (about 10 observations each day between 08:15 and 09:45 UT) with the reference data (one profile per day: 21 Jul 2013, 22 Jul 2013, 24 Jul 2013, 25 Jul 2013, 30 Jul 2013 and 31 Jul 2013).

Figure 3 shows the plots for the correlations between the reference and the FTIR data. The upper panel depicts the comparison for the lower free troposphere and the bottom panel for the middle free troposphere. The references are constructed from the in situ profile measurements (surface up to ceiling altitude of 6–7 km) and a climatology for higher altitudes by convolution with the FTIR averaging kernels. The climatology above the ceiling altitude is the same as the a priori data as discussed in Sect. 2.5. The technical details for this comparison, like the need for applying the averaging kernels to the reference profiles, are the same as for the exemplary study of Schneider et al. (2015). The error bars on the reference data are largely due to the unknown humidity and δD values above the aircraft's ceiling altitude. This can easily be understood from the averaging row kernels of the matrix blocks $\mathbf{A}_{11}^*$ and $\mathbf{A}_{22}^*$ as shown in Fig. 1. They reveal that the atmospheric state above 6–7 km does affect the retrieval for lower altitudes. Appendix C provides a brief discussion on the importance of reaching high ceiling altitudes.

Table 1. Empirical validation and bias assessment of the NDACC/FTIR H_2O and δD products in the lower troposphere.

Sensor	Altitude range	Number of remote sensing observations	Number of reference observation (N_R)	R^2/slope from fit H_2O	δD	Mean bias ± confidence H_2O (%)	δD (‰)
NDACC/FTIR	2.4–4 km	65	6	70 %/0.86	68 %/0.86	+2.1 ± 12.4	−12.1 ± 16.6

Table 2. Empirical validation and bias assessment of the NDACC/FTIR and MetOp/IASI H_2O and δD products in the middle troposphere.

Sensor	Altitude range	Number of remote sensing observations	Number of reference observation (N_R)	R^2/slope from fit H_2O	δD	Mean bias ± confidence H_2O (%)	δD (‰)
NDACC/FTIR	3–7 km	65	6	86 %/0.96	91 %/0.95	−0.8 ± 8.2	−2.7 ± 7.4
MetOp/IASI	2–8 km	10	4	97 %/0.89	88 %/0.74	+0.6 ± 3.7	+8.5 ± 7.9

We observe a reasonable correlation and no significant bias between the reference data and the MUSICA NDACC/FTIR v2015 data. We also see variations in the FTIR data measured between 08:15 and 09:45 UT on a single day, which cannot be attributed to changes in the averaging kernels because there is no similar variation seen in the smoothed reference data (there is only a single reference profile per day). This variation is seen in the lower free troposphere and in the middle free troposphere and is very likely a true variation in the free tropospheric humidity and δD fields.

The relatively high variability of the atmospheric state is a problem when comparing the different measurements because we do not know whether the different measurements detect air masses with the same atmospheric characteristics well. Our experience is that in the surroundings of Tenerife, the middle tropospheric humidity fields can be reasonably compared if they are made within 2 h (Schneider et al., 2010a, b) and within a horizontal distance of about 100 km (Wiegele et al., 2014). For these coincidence criteria, the mismatch between lower and middle tropospheric H_2O and δD can be assumed to be within 10 % and 10 ‰, respectively. However, the comparison of aircraft measurements (free troposphere) with measurements made at Izaña (on a mountain ridge) is more difficult due to the local thermal circulation that starts on the island during the morning hours (Schneider et al., 2010b; González et al., 2016). For that reason, we compare the in situ aircraft references with FTIR data measured in the early morning hours (between 08:15 and 09:45 UT) and define these measurements the optimal coincidences with the free tropospheric aircraft measurements made between 10:30 and 13:30 UT. As a consequence the mismatch uncertainty for the comparison between aircraft and FTIR data will be larger (within 30 % for H_2O and very likely within 30 ‰ for δD). For a detailed discussion on optimal coincidences between the aircraft-based in situ and the remote sensing measurements, please refer to Appendix C.

The Tables 1 and 2 resume the results of the empirical validation and bias assessment. The reference and the NDACC/FTIR products detect the same variations to a large extent (R^2 values of about 70 % for the lower and almost 90 % for the middle troposphere). The calculated mean NDACC/FTIR biases are not significant if we take the confidence range of these assessments into account. The confidence range is calculated as the standard deviation of the bias divided by $\sqrt{N_R - 1}$ (with N_R being the number of independent reference observations). For the lower troposphere, we are able to determine the bias with a confidence of 12.4 % and 16.6 ‰ for H_2O and δD, respectively. In the middle troposphere, the assessment is even more reliable. There, the confidence ranges are 8.2 % and 7.4 ‰ for H_2O and δD, respectively. These confidence ranges are in good agreement with the estimated mismatch uncertainties. In summary, the lower tropospheric bias is very likely somewhere between −10 and +15 % for H_2O and between −30 and +5 ‰ for δD. The middle tropospheric bias is very likely between −10 and +8 % for H_2O and between −10 and +5 ‰ for δD.

3.2 MetOp/IASI

In an exemplary study with the previous MUSICA MetOp/IASI retrieval version, Schneider et al. (2015) reported a bias between the IASI δD product and the δD reference of about 60 ‰ (see Fig. 11 therein). For the comprehensive bias assessment of the v2015 data, we follow the procedure as described in the context of that exemplary study.

Figure 4 shows the correlation plots between the reference and the MetOp/IASI v2015 data. The data points plotted by smaller symbols and by black error bars are for non-ideal coincidences, and the rest of the data points are for good coincidences (Appendix C gives more details on the coincidences and the error bars). For this comparison, we smooth the reference profile data (in situ measurements and climatological data above ceiling altitude, as described in Sect. 3.1) with the respective IASI averaging kernels. Since there is
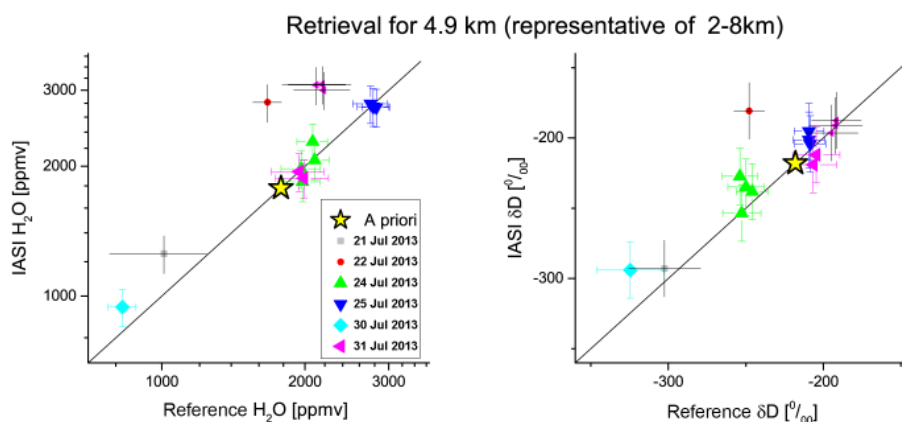
Figure 4. Same as Fig. 3 but for the correlation between reference data (in situ data measured by the ISOWAT instrument for 0–7 km and climatology above, then smoothed with IASI kernels) and IASI data for 5 km altitude. The colour code is for the different days. The data points for non-optimal coincidences as discussed in Appendix C can be identified by the smaller symbols and the black error bars.

only one reference profile per day, the small variations in the smoothed reference data on an individual day must be due to varying averaging kernels (for instance, the small variability of the green dots for 24 Jul 2013 in parallel to the x axis). The respective variations of the IASI data (variations in parallel to the y axis) are due to variations in the sensitivity of IASI (variation in the kernels) and due to variations in the real atmospheric state encountered at the different observational pixels. The in situ data and the remote sensing data observed for good coincidences are well correlated. We estimate a mismatch uncertainty of about 10 % and 10 ‰ for the H₂O and δD comparisons, respectively (for more details see discussions in Sect. 3.1 and Appendix C).

We are able to assess the bias for the middle tropospheric IASI data with a confidence of 3.7 % and 7.9 ‰ for H₂O and δD, respectively (see Table 2). The confidence ranges are in agreement with the expected mismatch uncertainties. The obtained mean bias values lie within these confidence ranges (for H₂O) or are only very slightly outside this range (for δD), meaning that the actual biases are very likely between -2.5 and $+5$ % for H₂O and between 0 and $+15$ ‰ for δD.

4 Validation of {H₂O,δD} pair distributions

An individual validation of H₂O and δD (as shown in the previous section) is important for documenting that the data are calibrated to the reference scales for H₂O and δD. However, it is not sufficient. It is the tropospheric {H₂O,δD} pair distribution that gives insight into tropospheric moisture pathways and therefore, it is the distribution of these pairs that has to be validated. Wiegele et al. (2014) and Schneider et al. (2015) presented approaches for such kinds of validation exercises. Here, we present a further refined {H₂O,δD} pair validation and compare in situ, MUSICA v2015 NDACC/FTIR, MUSICA v2015 MetOp/IASI-A and MUSICA v2015 MetOp/IASI-B data sets.

### 4.1 Moisture pathways to the North Atlantic subtropical free troposphere

In the surroundings of Tenerife there are three distinct moisture transport pathways that control free tropospheric humidity. González et al. (2016) showed that these three pathways have a distinct {H₂O,δD} pair distribution, which offers a unique opportunity for validating the different {H₂O,δD} pair data sets.

Generally, the free troposphere in the subtropics receives air that has been transported from higher latitudes and altitudes and subsides to the subtropics (e.g. Galewsky et al., 2005). In the following, we call this pathway "ATL, desc". However, the summertime free troposphere close to West Africa is often affected by the Saharan air layer (SAL). The SAL is a well-mixed planetary boundary layer that can expand up to 6–7 km and has its origin in the strong vertical mixing (dry convection) over the summertime Sahara. This dry convection process mixes boundary layer air with free tropospheric air. The SAL is then often advected westward over the Atlantic, where it can be identified by high dust concentrations (Rodríguez et al., 2011) and increased humidity levels. The free troposphere above Tenerife is also particularly humid when the air has been transported from lower altitudes over the tropical/subtropical Atlantic (González et al., 2016). This mainly occurs in the late summer and early autumn. We call this pathway "ATL, asc" in the following. The three distinct moisture transport pathways, their identification methods and the prevailing occurrences are summarized in Table 3 and discussed in great detail in González et al. (2016).

For our validation purpose we sort the {H₂O,δD} observations according to the moisture pathway that has been prevailing during the observation. The sorting is done according to the identification method as given in Table 3 and for all the different data sets independently: the Picarro

Table 3. The dominant moisture pathways to the free troposphere in the surroundings of Tenerife.

| Pathway	Description	Identification method	Season
ATL, desc.	Atlantic air mass descending from high latitudes	low aerosol load (measurement) and low temperature at point of last condensation (trajectories), González et al. (2016)	November–May
ATL, asc.	Atlantic air mass ascending from lower latitudes	low aerosol load (measurement) and high temperature at point of last condensation (trajectories), González et al. (2016)	July–October
SAL	Saharan air layer advected over the Atlantic	high aerosol load (measurement), Rodríguez et al. (2011); González et al. (2016)	July + August
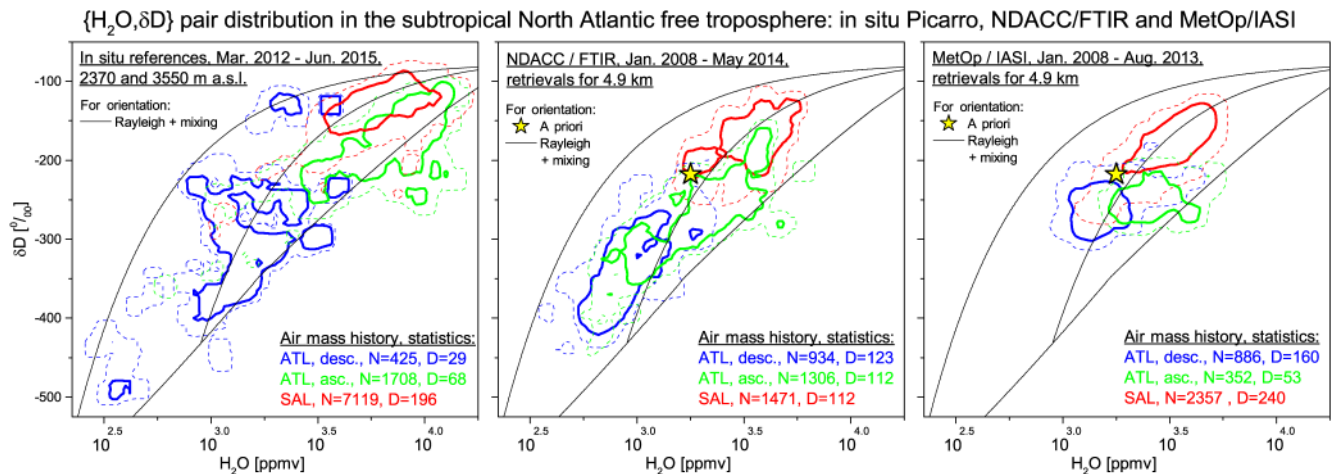
Figure 5. Free tropospheric {$H_2O, \delta D$} pair distributions as obtained by different measurement techniques in the surroundings of Tenerife (for orientation see also map as shown in Fig. C1). The contour lines indicate areas with the highest densities of the {$H_2O, \delta D$} pairs: red denotes air masses that are clearly affected by dry convection over the African continent; blue and green denote Atlantic air masses with different pathways (see Table 3). The thin dashed and thick solid lines mark the areas that include 95 % and 66 % of all data, respectively. Left: two Picarro in situ instruments (L2120-i) measuring during nighttime at 2390 and 3550 m a.s.l. (Izaña Observatory and Teide). Middle: ground-based NDACC/FTIR located at Izaña. Right: space-based MetOp/IASI-A and MetOp/IASI-B observing in a 2° × 2° area south of the island. In addition, the panels show three simulated curves (thin black lines): a Rayleigh curve for initialization with T = 25 °C, RH = 80 % and $\delta D = -80$ ‰ and two mixing curves (first line for mixing between $H_2O[1] = 25\,000$ ppmv; $\delta D[1] = -80$ ‰ and $H_2O[2] = 900$ ppmv; $\delta D[2] = -430$ ‰ and second line for mixing between $H_2O[1] = 25\,000$ ppmv; $\delta D[1] = -80$ ‰ and $H_2O[2] = 200$ ppmv; $\delta D[2] = -610$ ‰). The yellow star marks the a priori value used for the remote sensing retrievals at 4.9 km.

surface-based in situ observations (at 2390 and 3550 m a.s.l.), the NDACC/FTIR measurements made from Izaña and the MetOp/IASI observations made close to Tenerife. Then we calculate the {$H_2O, \delta D$} pair density distribution for each observational technique and each moisture pathway ensemble. The results are the {$H_2O, \delta D$} pair contour plots as depicted in Fig. 5 (from the left to the right for the different data sets as described in the panels). We present these plots on a logarithmic scale for H_2O and maintain the scale for δD (the δD scale is in a first approximation the same as a $\ln[HDO] - \ln[H_2O]$ scale). These are the scales on which the optimal estimation of the remote sensing products is performed. This largely facilitates the interpretation of the remote sensing data because then the Type 2 kernels are very similar on the x and y scales. Furthermore, on these scales a Rayleigh process will become visible by a straight line.

For air descending from the Northern Atlantic (ATL, desc, blue contours), the data points are well distributed between a typical Rayleigh line (gradual dehydration due to condensation) and mixing lines (mixing of two end members with {$H_2O, \delta D$} on the exemplary Rayleigh line). These water masses have gone through different condensation and mixing processes.

For air ascending from the tropical/subtropical Atlantic (ATL, asc, green contours), the air is more humid and the {$H_2O, \delta D$} pairs generally group around the Rayleigh line with some data points lying significantly below the Rayleigh line. These water masses are strongly depleted in HDO, which indicates rain re-evaporation or gradual dehydration (Rayleigh distillation) after evaporation over a warm ocean.

For SAL conditions (red contours), the air is also humid but HDO is significantly enriched when compared to the typical Rayleigh distribution. This can be well explained by
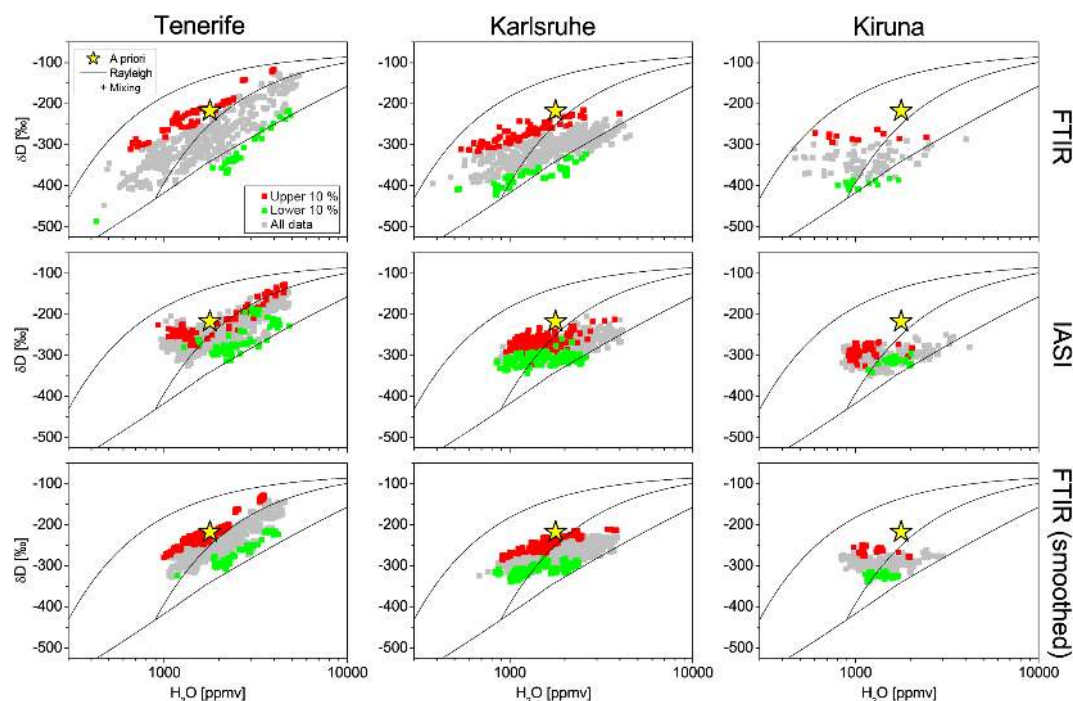
Figure 6. {H₂O,δD} pair plots for 4.9 km altitude for coincident FTIR and IASI measurements for the three locations: Tenerife, Karlsruhe, and Kiruna. The FTIR data, the IASI data and FTIR data smoothed with the IASI averaging kernels are plotted (from the top to the bottom). The colour code displays the upper 10 % and lower 10 % of δD values as identified in the FTIR data. The black lines and the yellow stars are the same as in Fig. 5 (Rayleigh line, mixing lines and a priori value for 5 km altitude, respectively). For more details on this kind of validation approach, please refer to Wiegele et al. (2014).

the mixing of planetary boundary layer humidity with middle/upper tropospheric humidity.

We observe that the three different data sets reveal very similar {H₂O,δD} pair distributions depending on the history of the detected air mass. The study is statistically very robust, since it uses several hundred individual observations (number given by parameter N in the legends of Fig. 5) made on many different days (number given by parameter D). This confirms that the v2015 MUSICA remote sensing data are reasonably well bias corrected and proves that they are capable of tracking different moisture pathways. The smaller variability in the remote sensing data is due to the fact that they represent averages for layers of several kilometres (see averaging kernel plots of Figs. 1 and 2). For the MetOp/IASI data the variability is particularly small for dry air (blue contours) because the drier the atmosphere, the lower IASI's sensitivity for middle tropospheric {H₂O,δD} pairs.

4.2 {H₂O,δD} extremes on global scale

Figure 5 shows validations of {H₂O,δD} pairs for a subtropical site. In order to perform a similar study for other sites, we would need respective middle tropospheric in situ references, which are not available. The ISOWAT profile and surface-based Izaña and Teide Picarro in situ references as observed in the surroundings of Tenerife are unique and a

generation of similar data sets for middle or high latitudes would be expensive (it would require a large number of aircraft campaigns).

Here, we show a comparison between NDACC/FTIR, MetOp/IASI-A and MetOp/IASI-B, which is of global validity. Our argument is that a global agreement between the different remote sensing data sets would suggest that the in situ validations made for Tenerife are of global validity.

For this kind of validation, we work with {H₂O,δD} extremes. For this purpose, we identify anomalous or extreme {H₂O,δD} distributions in one remote sensing data set and document to what extent these extremes are seen in another remote sensing data set (by comparing coincident observations). The validation approach with {H₂O,δD} extremes was first presented by Wiegele et al. (2014), which should be consulted for more details.

4.2.1 NDACC/FTIR vs. MetOp/IASI

We compare the FTIR and IASI data for three rather different sites: Tenerife (subtropical Atlantic), Karlsruhe (central Europe) and Kiruna (northern Scandinavia). At these sites, we have ground-based FTIR observations of NDACC that contribute to MUSICA and we performed continuous IASI retrievals around the FTIR locations. Figure 6 shows the {H₂O,δD} distributions as retrieved at the three sites from
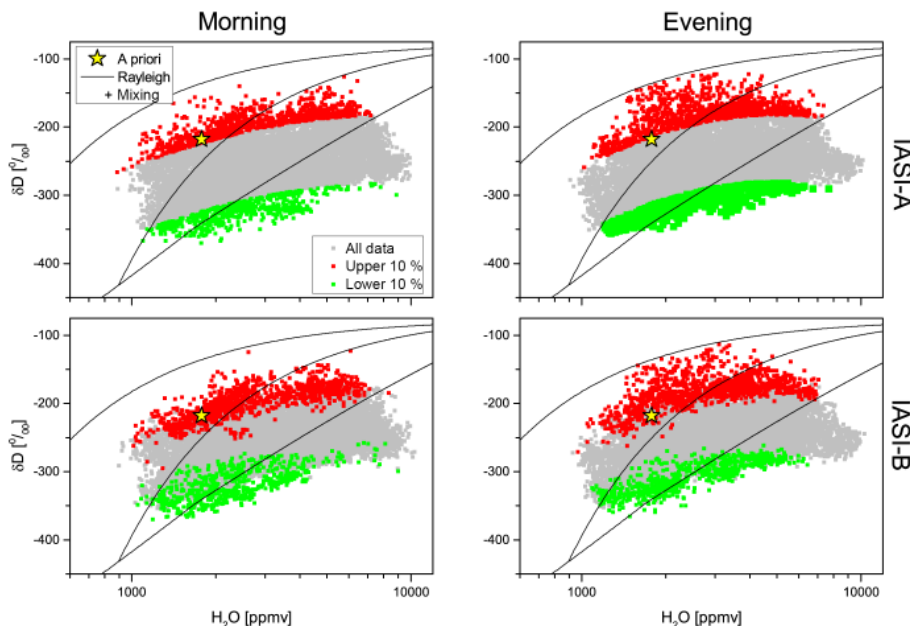
Figure 7. Similar to Fig. 6 but for coincidences of IASI-A and IASI-B measurements. The products retrieved at 4.9 km for all coincidences within 1 h and $0.25° \times 0.25°$ are presented for 16 August 2014. The left panels show the morning overpasses and right panels the evening overpasses. The anomalies are identified in the IASI-A observations (upper panels) and then checked in the IASI-B observations (bottom panels).

coincident FTIR and IASI measurements (IASI observations made in an 110×110 km area south of the FTIR instruments). As temporal coincidence criterium we required that the two measurements were made within 1 h. The left column of plots shows data for Tenerife (coincidences between 2007 and 2013), the central column data for Karlsruhe (coincidences between 2010 and 2013) and the right column data for Kiruna (coincidences between 2007 and 2012). The first row of plots depicts the FTIR data, the second row of plots shows the IASI data and the third row of plots the FTIR data smoothed by the IASI averaging kernels. In all plots we show retrievals for 4.9 km altitude. The grey data points represent all data. The FTIR observations that show unusual low or strong HDO depletion (high or low δD values) are marked in red and green, respectively. These anomalies or extremes have been identified by a second-order least squares fit to the {ln[H₂O],δD} distribution. The 10 % of the data points that have the largest positive/negative δD difference to the regression curve are defined as the extreme values.

First, comparing the {H₂O,δD} distribution relative to the unique a priori point, we see a good agreement between both data sets. In both data sets and from Tenerife via Karlsruhe to Kiruna, the water masses get generally more and more depleted in HDO and the {ln[H₂O],δD} slopes become more and more shallow. Second, both data sets reveal very similar anomalies. If the FTIR observes an anomalously weak depletion, IASI also does (red dots in the IASI plots are situated at the upper end of the δD distribution). The same is true for the anomalies with strong depletion (green dots).

In summary, the {H₂O,δD} distribution patterns (latitudinal gradients, {ln[H₂O],δD} slopes, anomalous distributions) as observed in the MUSICA NDACC/FTIR and MUSICA MetOp/IASI data are in good agreement. This finding suggests that the {H₂O,δD} pair validation as shown in the previous sections for the surroundings of Tenerife is valid for very different geophysical locations.

4.2.2 IASI-A vs. IASI-B

Since 2013 two IASI instruments (A and B) on two different satellites (MetOp-A and MetOp-B) have provided operational spectra. Their respective overpasses take place typically within 30 min, which offers very good conditions for cross-validating the IASI-A and IASI-B products.

Figure 7 depicts {H₂O,δD} distributions considering all valid observations on 16 August 2014 (left columns for the morning overpass and right columns for the evening overpass). The colour code is the same as in Fig. 6. The grey data points show all data, the red data points mark the observations that have been identified in the IASI-A data as a positive δD extreme and the green data points mark the observations that correspond to a negative IASI-A δD extreme.

The top panels show the IASI-A data. These data are used for identifying the extremes and the red and green data points are of course separated. The bottom panels show the IASI-B data and green and red mark the IASI-B observations that are conducted in coincidence with the extreme IASI-A observations. The coincidence criteria were measurements within 1 h

Table 4. List of current MUSICA NDACC/FTIR sites (ordered from north to south) and available MUSICA data record of quality-filtered data. DOFS (degrees Of freedom of signal) for the optimal estimation of {H$_2$O,δD} pairs (trace of $\mathbf{A}_{11}^* \approx \mathbf{A}_{22}^*$; an example of these matrix blocks is plotted in Fig. 1). This table is adopted from Barthlott et al. (2016a).

Site	Location	Altitude	Data record	No. of meas. (N)	Meas. days (D)	DOFS
Eureka, Canada	80.1° N, 86.4° W	610 m a.s.l.	2006–2014	1890	398	1.7
Ny Ålesund, Norway	78.9° N, 11.9° E	21 m a.s.l.	2005–2014	730	251	1.6
Kiruna, Sweden	67.8° N, 20.4° E	419 m a.s.l.	1996–2014	1981	969	1.6
Bremen, Germany	53.1° N, 8.9° E	27 m a.s.l.	2004–2014	582	316	1.6
Karlsruhe, Germany	49.1° N, 8.4° E	110 m a.s.l.	2010–2014	1756	425	1.6
Jungfraujoch, Switzerland	46.6° N, 8.0° E	3580 m a.s.l.	1996–2014	1884	1175	1.6
Izaña/Tenerife, Spain	28.3° N, 16.5° W	2367 m a.s.l.	2001–2014	9350	1210	1.7
Altzomoni, Mexico	19.1° N, 98.7° W	3985 m a.s.l.	2012–2014	1489	234	1.7
Addis Ababa, Ethiopia	9.0° N, 38.8° E	2443 m a.s.l.	2009–2013	528	154	1.6
Wollongong, Australia	34.5° S, 150.9° E	30 m a.s.l.	2007–2014	5834	927	1.6
Lauder, New Zealand	45.1° S, 169.7° E	370 m a.s.l.	1997–2014	3533	1653	1.6
Arrival Heights, Antarctica	77.8° S, 166.7° E	250 m a.s.l.	2002–2014	374	287	1.4

and within an area of 0.25° × 0.25°, whereby the compared IASI-A and IASI-B data are often measured with rather different swath angles. We find that IASI-B detects very similar δD extremes as IASI-A, which demonstrates the good global consistency of the IASI-A and IASI-B {H$_2$O,δD} pairs, the robustness of the retrieval (compared are observations with different swath angles) and that our coincidence criteria used in the context of Sect. 3 are reasonable. In summary, we can use the IASI-A and IASI-B products as a uniform and consistent {H$_2$O,δD} pair data set.

5 Consistent long-term observation with NDACC/FTIR

Ground-based FTIR high-resolution solar absorption spectra have been measured within the NDACC for many years and can be used for generating long-term data sets of tropospheric {H$_2$O,δD} pairs (Schneider et al., 2012). For MUSICA, the principal investigators of the individual FTIR stations send the spectra to the MUSICA retrieval team where they are centrally evaluated. This strategy assures highest consistency between the retrieval products for the different stations.

The NDACC/FTIR activities complement the surface-based in situ isotopologue monitoring activities. While the data obtained from the latter represent near-surface small-scale variations, which are often difficult for models to capture, the MUSICA NDACC/FTIR isotopologue data are representative of different altitudes and for processes that take place over deeper layers (the data represent vertical layers averaged over 2–5 km; see typical averaging kernels in Fig. 1). Due to their long-term data characteristics, the NDACC/FTIR data are particularly interesting for climatological studies.

5.1 Contributing stations and currently available data volume

The number of stations contributing to the MUSICA activities is gradually increasing and the data sets have been updated. Table 4 gives an overview of the 12 NDACC/FTIR sites that currently contribute to the MUSICA activities and the available data records. The stations are well distributed from the Arctic to the Antarctic and in some occasions have provided data since the late 1990s (a plot of time series until 2012 is given in Fig. 12 of Schneider et al., 2012). A further extension of the data set to other sites or for some stations to measurements made in the beginning of the 1990 is feasible, but has not been possible with the funds available for the MUSICA project.

5.2 Data filtering

All the data pass through a quality filter with different criteria. First, we require total DOFS for the three water vapour isotopologues (H$_2^{16}$O, HD^{16}O and H$_2^{18}$O) of at least 4.0. Second, we analyse the position of solar lines with respect to terrestrial lines and require a $\Delta\nu/\nu$ within 5×10^{-6} ($\Delta\nu$ is the difference in the line shift of solar and terrestrial lines and ν the position of the solar line, both given in cm^{-1}). This method allows observations made with incorrect pointing of the solar tracker to be excluded (Gisi et al., 2011). Third, we require that the fitted phase error of the instrumental line shape does not change by more than 0.02 rad during the period of the data record. Thereby, we exclude data that have been measured under anomalous instrumental characteristics. Fourth, we perform XCO$_2$ retrievals using the same spectra as for the water vapour isotopologue retrievals. We compare the retrieved XCO$_2$ values with XCO$_2$ as obtained from a multi-parameter model for XCO$_2$ (Barthlott et al., 2015). We require that the measured and modelled XCO$_2$ data agree within 2 %.
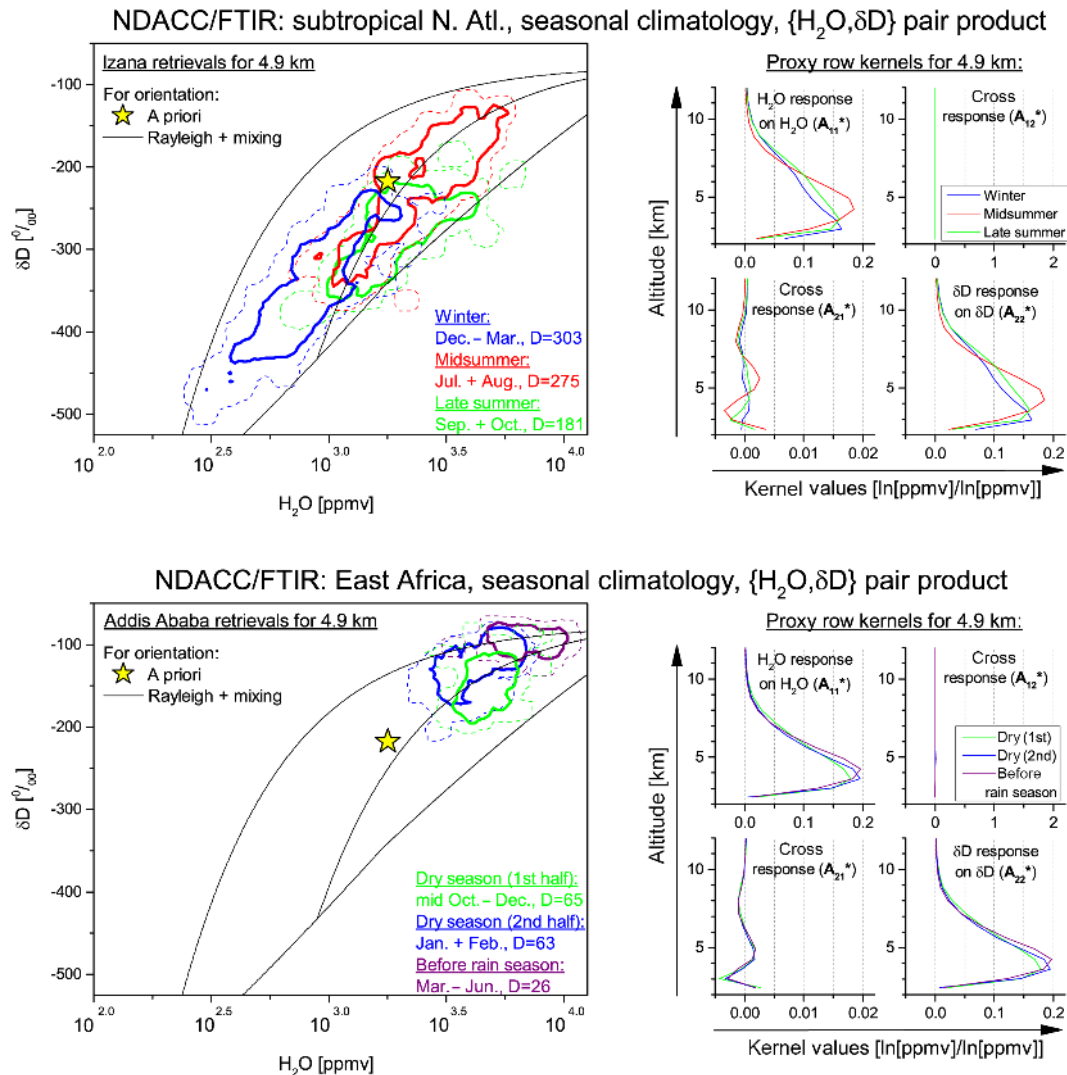
Figure 8. Example of seasonal {H$_2$O,δD} pair distribution climatologies obtained from FTIR retrievals for 4.9 km at Izaña/Tenerife (top panels) and Addis Ababa (bottom panels). The left panels show the distribution density plots, whereby the thin dashed and thick solid lines mark the areas that include 95 and 66 % of all data, respectively. The different colours correspond to the seasons as explained in the legends. The yellow star and black lines are the a priori and the simulated lines as in Figs. 5 and 6. The right panels show corresponding typical row kernels for 4.9 km for the H$_2$O and δD proxies as well as for their cross-responses (for more general details about the FTIR kernels, see Fig. 1 and corresponding discussions).

5.3 Seasonal {H$_2$O,δD} climatologies

Figure 8 gives an example of the seasonal cycles in the {H$_2$O,δD} distributions (around 5 km altitude) obtained from the observations made on Tenerife in the subtropical North Atlantic (14 years: 2001–2014) and in Addis Ababa in East Africa (4 years: 2009–2013).

For the subtropical North Atlantic (upper panels), the seasonal cycle can be explained by the seasonality of the prevailing moisture pathways as summarized in Table 3, so the {H$_2$O,δD} pair distribution plot shown here is very similar to the one shown in Fig. 5 (central panel). The right panels show typical row kernels for the three different seasons and

for the altitude of 4.9 km. Due to the a posteriori processing, the sensitivity with respect to H$_2$O and δD is almost identical (compare row kernels of $\mathbf{A}_{11}^*$ and $\mathbf{A}_{22}^*$). However, the sensitivities slightly depend on the season. It seems that during winter and late summer the 4.9 km retrieval is more sensitive to the lower troposphere than to the middle troposphere, whereas the situation is vice versa for retrievals of midsummer observations.

Over East Africa (bottom panel) the air is generally more humid and less depleted in HDO than over the subtropical North Atlantic. Furthermore, we observe different {H$_2$O,δD} distributions for the different seasons. Directly after the rain season (mid-October–December, green contours) the vapour
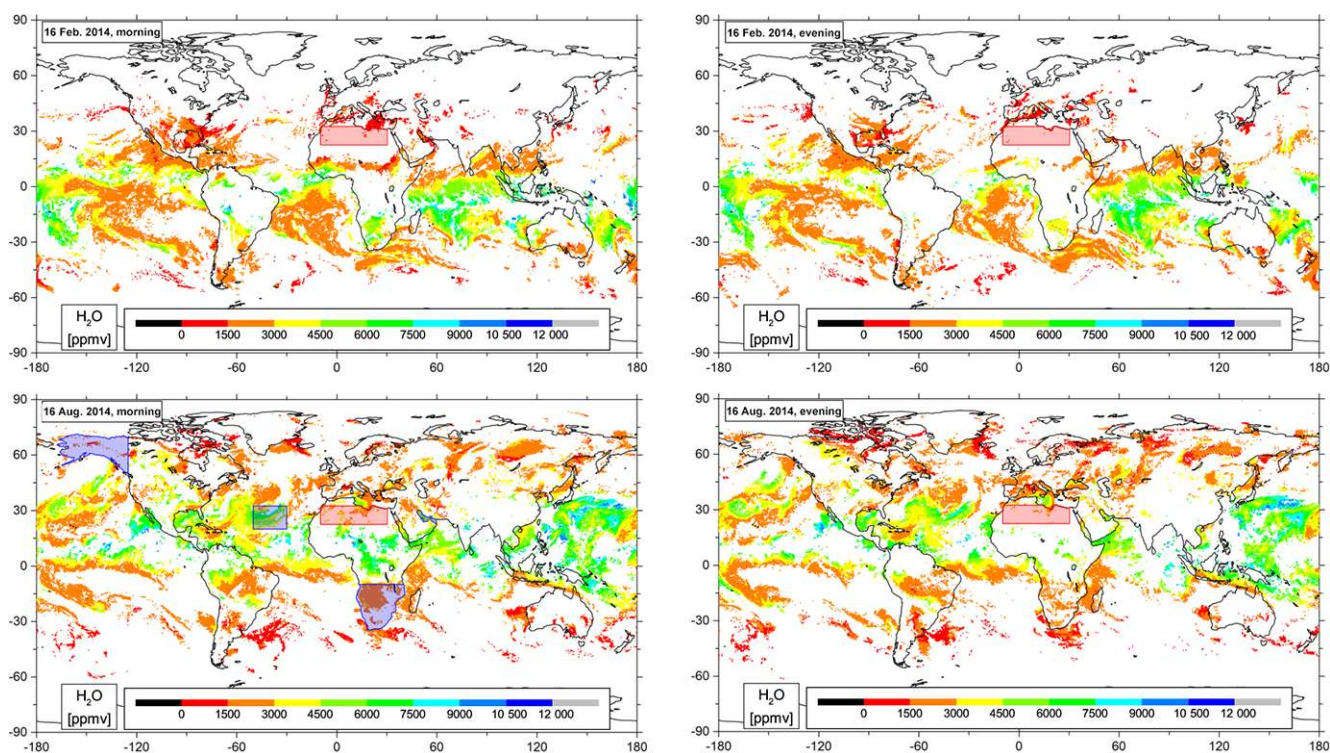
Figure 9. Daily morning and evening coverage for the MUSICA IASI-A and IASI-B Type 2 retrieval product that passed the sensitivity filter (Eq. 5) for 4.9 km altitude and the retrieval quality filter. Left panels show the morning overpass and the right panels show the corresponding evening overpass. Top panels are for a typical situation during northern winter (example 16 February 2014) and bottom panels for northern summer (example 16 August 2014). The marked areas (blueish and reddish) are discussed in detail in the context of Fig. 10.

is most depleted in HDO. In January and February (blue contours) the air remains similarly dry, but becomes more enriched in HDO. Then, before the rain season (March–June, purple contours), the air gets more humid, but δD gets only slightly enriched in HDO. The typical row kernels depicted in the right panels, reveal very similar sensitivities for all the different seasons.

The main intention of this figure is to briefly demonstrate the potential of the NDACC/FTIR data for climatological {H$_2$O,δD} pair distribution analyses. A deeper scientific discussion of the climatological signals would need model calculations and is beyond the scope of this paper.

# 6 Quasi-global and high-resolution observations with MetOp/IASI

IASI sensors are aboard the MetOp satellites, which is a series of three satellites (MetOp-A, MetOp-B and MetOp-C) for covering the time period from 2006 to the beginning of the 2020s. MetOp has 14 orbits per day at about 817 km altitude, which, together with the swath width of about 2200 km of the IASI instruments, leads to a quasi-global coverage of morning overpasses (at about 10:00 LT) as well as evening overpasses (at about 22:00 LT). The swath angles are be-

tween 0° (nadir) and 48.3°, whereby the ground pixel at nadir has a diameter of 12 km. MetOp-A with IASI-A was launched in October 2006 and MetOp-B with IASI-B in September 2012. Currently, both IASI instruments are operative.

6.1 Spatial and temporal resolution, coverage and currently available data volume

For one morning or evening overpass the IASI-B swaths typically complement the area left out by the IASI-A swaths, and vice versa. Since the MUSICA IASI-A and IASI-B data are very consistent (see Fig. 7), we can treat them as a uniform data set and create extremely dense global data point maps for each daily morning and evening overpass. Figure 9 depicts typical maps for single day morning and evening overpasses during boreal winter and summer, respectively. The areas with missing data are cloudy areas or correspond to scenarios where the retrieval has rather low sensitivity.

Currently, MUSICA MetOp/IASI-A and MetOp/IASI-B data (Type 1 and Type 2 products) are available on a global scale for 6 days in February 2014 and for the whole months of August 2014. In addition, we have retrievals' results for longer time periods and for $2° \times 2°$ areas around the three ground-based FTIR sites, Izaña (Tenerife), Karlsruhe and
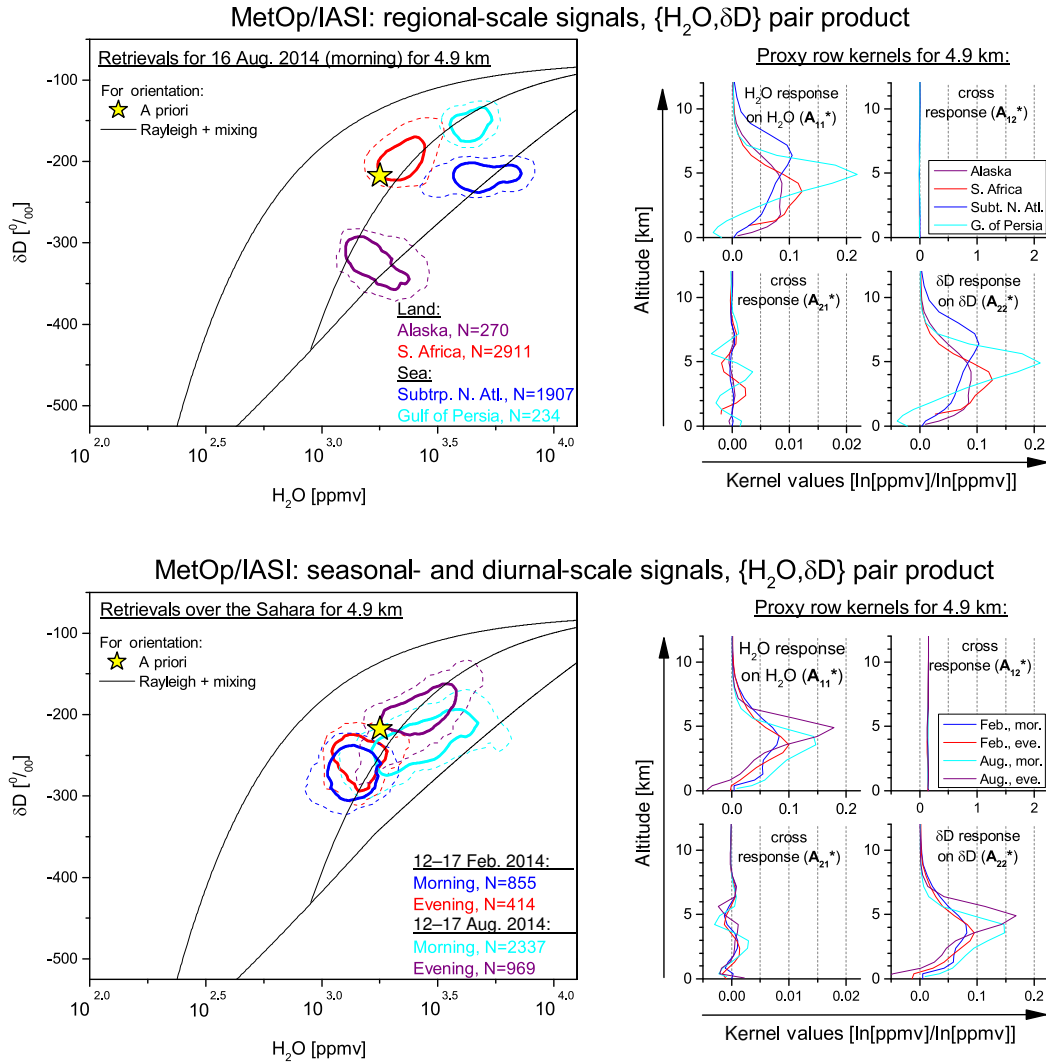
Figure 10. Example of regional-scale signals (top panels), and seasonal- and diurnal-scale signals (bottom panels) in the {H$_2$O,δD} pair distribution as obtained from IASI-A and IASI-B spectra. The left panels show the distribution density plots for retrieval results of 4.9 km, whereby the thin dashed and thick solid lines mark the areas that include 95 and 66 % of all data, respectively. The different colours correspond to the regions, seasons and daytime as marked in Fig. 9 and as explained in the legends. The yellow star and black lines are the a priori and the simulated lines as in Figs. 5, 6 and 8. The right panels show the corresponding typical row kernels for 4.9 km for the H$_2$O and δD proxies as well as for their cross-responses (for more general details about the IASI kernels, see Fig. 2 and corresponding discussions).

Kiruna. More MUSICA MetOp/IASI retrievals are planned, but depend on future funding.

6.2 Sensitivity and retrieval quality filter

The height region around 5 km altitude (about 500 hPa) is generally most sensitive with respect to the {H$_2$O,δD} pairs. However, occasionally (e.g. for an extremely dry or humid troposphere) the sensitivity peaks at other altitudes.

To filter out data with low sensitivity at a certain altitude, we set up a matrix in representation of the atmospheric co-variances (the matrix's elements represent the different altitude levels). This matrix ($\mathbf{S}_c^*$) has unity values on the diago-

nal, and the outer diagonal elements are obtained by assuming an inter-level correlation length of 5 km. Then we calculate the error covariance in the retrieved data as

$$\mathbf{S}_\epsilon^* = (\mathbf{A}^* - \mathbf{I})\mathbf{S}_c^*(\mathbf{A}^* - \mathbf{I})^T. \tag{5}$$

Here, $\mathbf{A}^*$ is the averaging kernel matrix (see Eq. 4 and Fig. 2 for an example) and $\mathbf{I}$ the identity matrix. If we are interested in data that represent the atmosphere at altitude X, we do not consider retrievals, for which the respective diagonal element of $\mathbf{S}_\epsilon^*$ is larger than 0.5^2, thereby requiring that at least 50 % of the atmospheric variation at altitude X is seen in the retrieved data. In Fig. 9 we only plot data points for which this sensitivity criterion is fulfilled for the altitude of 4.9 km (i.e.

it only shows data that reflect variations of a relatively deep layer at about 5 km altitude).

We filter out poor quality observational data by only considering retrievals for which the root mean square value of the residuals (difference between measured and simulated radiances) relative to the maximum value of the radiances is smaller than 0.0065.

The cloud, retrieval quality and sensitivity filter for 4.9 km altitude leaves us with about 120 000 and 110 000 valid data points for each single morning and evening overpass in August, respectively. In February there are typically 100 000 and 95 000 valid morning and evening observations for each day, respectively. Each of these data points represents the middle tropospheric situation of a small area (12 km diameter at nadir).

6.3 Regional-scale signals

In order to demonstrate the high potential of IASI for a daily detection of regional-scale moisture transport pathways, we analyse the {H$_2$O,δD} pair distribution measured on 16 August 2014 in different regions during the morning overpass. We investigate observations over land (two distinct locations: Alaska and South Africa) and sea (two distinct locations: subtropical North Atlantic and Gulf of Persia). The analysed regions are marked by a bluish colour in Fig. 9 and the respective {H$_2$O,δD} pair density distributions are plotted in the upper left panel of Fig. 10.

IASI detects very distinct {H$_2$O,δD} pair distributions for the different regions. The air over Alaska and South Africa is similarly dry; however, the δD values differ systematically by more than 150 ‰. A look on the row kernels (right panels) reveals that in both regions, IASI has a very similar sensitivity, which peaks between 2 and 5 km altitude. An apparent explication is that in Alaska, the drying happens by condensation (via Rayleigh distillation), while in South Africa, the drying is due to mixing with very dry air (subsidence from the upper troposphere).

The air over the North Atlantic and the Gulf of Persia is similarly humid, but there is a clear difference in δD. A reason for the difference in δD might be that over the North Atlantic, rain re-evaporation is important, whereas the air over the Gulf of Persia is strongly affected by dry convection processes (vertical mixing) over the Arabian peninsula. The row kernels for both scenes are not the same however, both show peak sensitivities for altitudes between 4 and 8 km, meaning that for both regions, IASI should be able to consistently capture variations in the {H$_2$O,δD} pair distributions that take place within a deep middle tropospheric layer.

6.4 Seasonal- and diurnal-scale signals

The bottom panels of Fig. 10 demonstrate IASI's potential for detecting seasonal- and diurnal-scale signals in the {H$_2$O,δD} pair distribution. This is done by analysing the

{H$_2$O,δD} pair distributions over the Sahara (22.5 to 32.5° N and 10° W to 30° E, region marked by a reddish colour in Fig. 9) for six consecutive winter and summer days and for morning and evening overpasses. Morning overpasses of the IASI instruments are at about 10:00 LT and evening overpasses at about 22:00 LT.

In the context of Fig. 5 we discussed the SAL events that can be observed during July and August over the Atlantic Ocean. Actually, the dry convection process that is responsible for the distinct {H$_2$O,δD} pair distribution under SAL conditions in the surroundings of Tenerife takes place over the Sahara. The strong heating of the Earth's surface during the day in summer is the main driver of these processes, which should be manifested by a pronounced diurnal cycle over the Sahara in August. Indeed, for August we observe such diurnal signals in the MUSICA {H$_2$O,δD} pair data. For the morning overpasses we observe a fractionation that is similar to the situation in winter (δD values between -300 and -200‰), whereas for the evening overpass the δD values veer away from the Rayleigh line and group around a line that simulates mixing between the planetary boundary layer air and middle free tropospheric air (δD values between -250 and -140‰). This evening distribution is very similar to the distribution that IASI typically observes over the Atlantic under SAL conditions (red contours in the right panel of Fig. 5). For February, the surface heating is much weaker than in summer and dry convection processes are unlikely. As a result, we observe no significant difference between the morning and evening {H$_2$O,δD} pair distribution.

Regarding the morning data, the moistening from winter to summer does not happen perfectly parallel to a Rayleigh line. This is probably because in summer the evaporation takes place over a warmer ocean than in winter and we have to consider different Rayleigh lines for winter and summer.

The main intention of Fig. 10 is to give examples of the large potential of IASI {H$_2$O,δD} products. A more profound scientific study of these {H$_2$O,δD} pair distribution patterns can only be done with model calculations and is out of the scope of this paper.

7 Defective interpretation of H$_2$O and δD remote sensing data

The previous sections have demonstrated the feasibility of the remote sensing of {H$_2$O,δD} pair distributions. In this context, it is important to recall that so far we have only presented examples of {H$_2$O,δD} pair distributions using a posteriori processed remote sensing products (thereby assuring the same sensitivities for H$_2$O and δD; see right panels in Figs. 8 and 10). In this section, we will briefly discuss the difficulty of correctly interpreting the distribution of the {H$_2$O,δD} pairs obtained from remote sensing data that are not a posteriori processed, which is the type of data that are typically provided by other data producers.
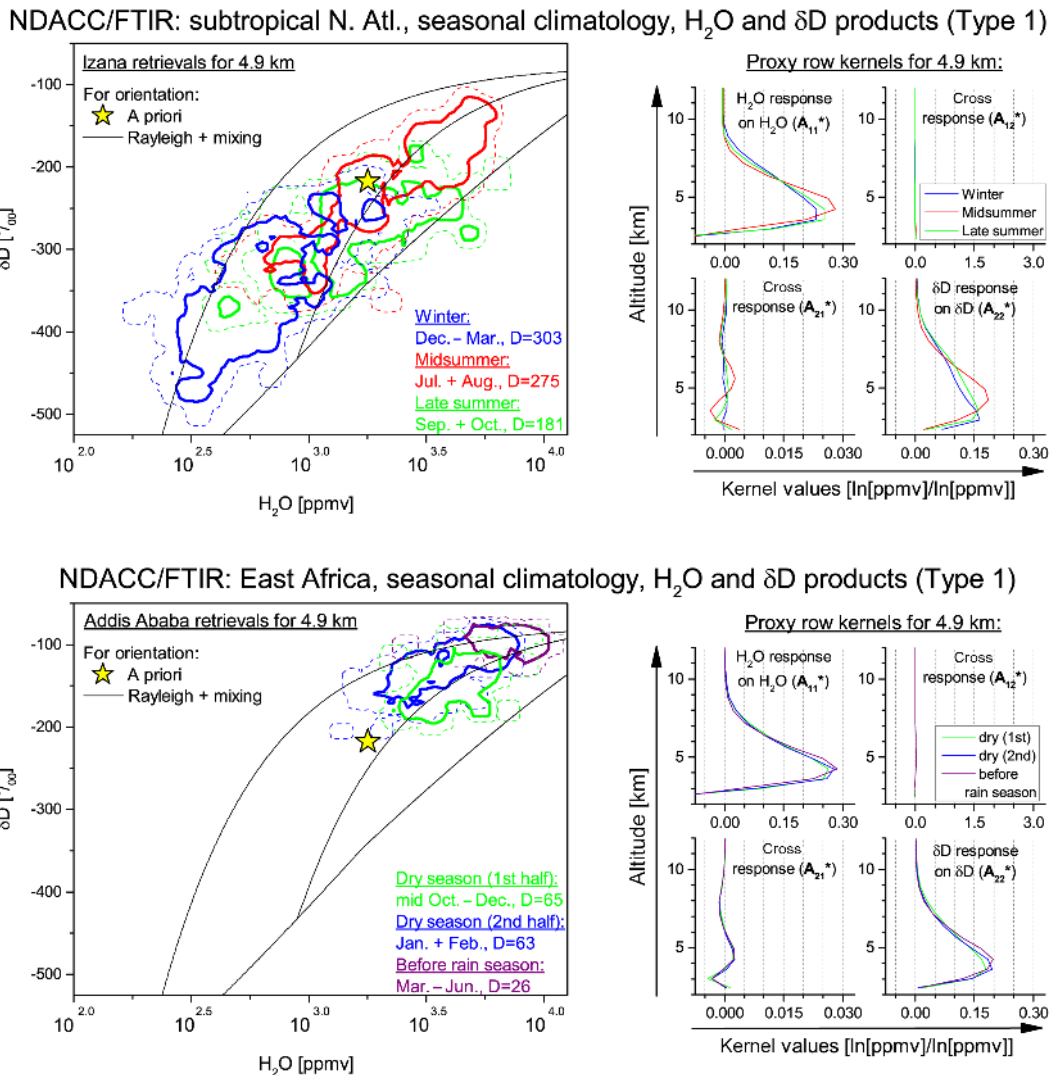
Figure 11. Same as Fig. 8, but instead of the {$H_2O, \delta D$} pair product (a posteriori corrected product), the plots are for the direct H_2O and δD retrieval output (Type 1, no a posteriori correction). Please note the different scale on the x axis of the row kernel plots compared to Fig. 8.

7.1 Discussion of example cases

Figure 11 shows exactly the same as Fig. 8, but for data that have not undergone the a posteriori processing. In MUSICA we call them the Type 1 products and they represent individual optimal estimations of H_2O and δD. For the Type 1 product, H_2O and δD are not sensitive for the same air mass and the retrieval response is much more sensitive to atmospheric H_2O than to δD variations. This is revealed by the typical row kernels as depicted on the right panels. There is clearly a higher sensitivity for H_2O than for δD (compare the row kernels of the matrix blocks $\mathbf{A}_{11}^*$ and $\mathbf{A}_{22}^*$).

The different sensitivities affect the slopes in the {$H_2O, \delta D$} distribution plots. Concretely, the NDACC/FTIR Izaña Type 1 data for winter (blue contour lines in upper panel of Fig. 11) show a {$H_2O, \delta D$} pair distribution

where dry air can occasionally be weakly depleted (significant number of data points with H_2O concentrations below $10^{2.7}$ ppmv ≈ 500 ppmv and δD above -400‰). It is very likely that these data points only appear there because of the H_2O sensitivity being higher than the δD sensitivity. Actually, when accounting for the different H_2O and δD sensitivities, this observation is not made (see Fig. 8). For midsummer, the Type 1 data show a {$H_2O, \delta D$} pair distribution that is reasonably parallel to a Rayleigh line (red contour lines in upper left panel of Fig. 11), whereas the distribution when H_2O and δD have almost identical sensitivities is more along a mixing line (red contour lines in upper left panel of Fig. 8).

Concerning East Africa (lower panel of Fig. 11), the Type 1 {$H_2O, \delta D$} pairs are generally distributed around a line with a slope being less steep than the slope of a Rayleigh line. However, the conclusion that mixing with dry air is the
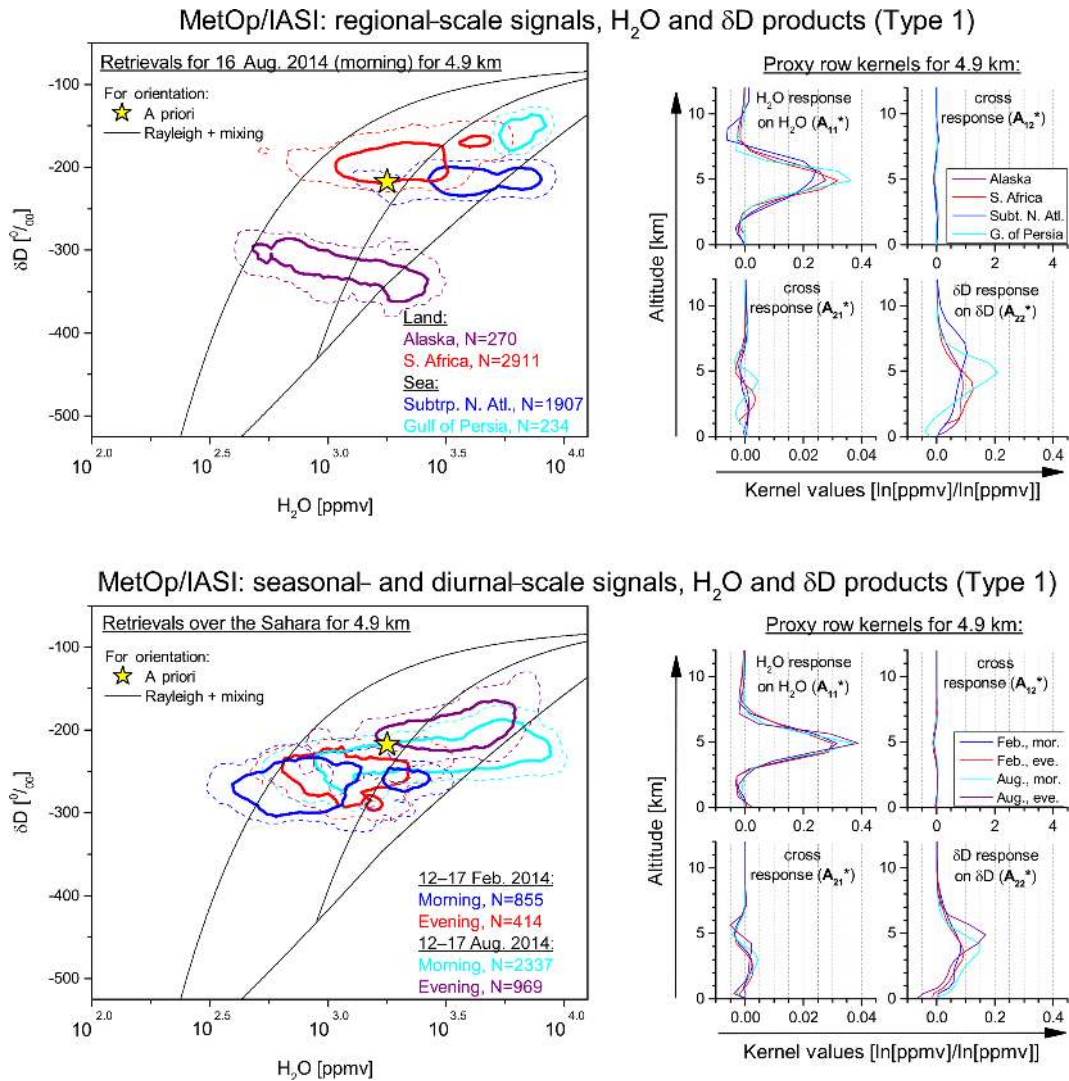
Figure 12. Same as Fig. 10, but instead of the {H_2O,δD} pair product (a posteriori corrected product), the plots are for the direct H_2O and δD retrieval output (Type 1, no a posteriori correction). Please note the different scale on the x axis of the row kernel plots compared to Fig. 10.

dominating drying process might be wrong because when analysing the a posteriori processed {H_2O,δD} pair distribution, the slope is steeper and in parallel to a Rayleigh line (see Fig. 8).

The risk of such defective interpretations is larger the more pronounced the difference between the H_2O and δD sensitivities is. For the MetOp/IASI products the sensitivity difference is especially important. Figure 12 shows exactly the same as Fig. 10, but for data that have not undergone the a posteriori processing. We observe completely changed {H_2O,δD} pair distribution patterns. These changed patterns reveal the risk of a defective interpretation of the real atmospheric situation when using H_2O and δD data that have significantly different averaging kernels. The row kernels are

plotted in the right panels, and the very different entries in the matrix blocks $\mathbf{A}_{11}^*$ and $\mathbf{A}_{22}^*$ can be clearly observed.

The cyan contour lines in the upper panel of Fig. 12 are reasonably close to the exemplary Rayleigh line. This means that the moisture above the Gulf of Persia might be defectively interpreted as being partly dried by Rayleigh distillation processes. This is in contrast to what is indicated by the more reliable {H_2O,δD} pair distribution pattern from Fig. 10. There the cyan contour lines are close to a mixing line, revealing that mixing with dry air is actually much more important than dehydration by condensation. Vice versa, for Alaska a δD value of -300‰ for H_2O concentrations below $10^{2.8}$ ppmv ≈ 630 ppmv (see purple contour lines in the upper panel of Fig. 12) indicates drying by mixing with dry air; however, when considering the different sensitivities in H_2O

and δD it seems that drying by mixing is rather unlikely. Instead, dehydration by condensation is suggested (see corresponding contour line in Fig. 10).

A further example for defective interpretations is the seasonal cycle over the Sahara. The {H$_2$O,δD} pair distributions as depicted in the bottom panel of Fig. 12 suggest strong differences between the summer and winter humidity levels, but only small differences in δD. Whereas during summer the {H$_2$O,δD} pairs are reasonably close to the exemplary Rayleigh line, they are far away from this line in winter. When removing the inconsistencies between the H$_2$O and δD sensitivities, this behaviour is very different. Then, the seasonal variation happens much closer to the exemplary Rayleigh line (see bottom panel of Fig. 10).

Already the few examples discussed here clearly demonstrate that the interpretation of {H$_2$O,δD} pair remote sensing data has to be done with great care. It is important to have a look at the sensitivities of H$_2$O and δD (as well as at their cross-sensitivities). The transformation of the {H$_2$O,δD} proxy basis system helps to gain insight into the complex characteristics of these remote sensing data products (see the discussions in Sect. 2 and the references cited therein). In order to reduce the risk of defective data interpretation, we strongly recommend the a posteriori data processing, which provides {H$_2$O,δD} pair distributions that can be interpreted in a straightforward manner (see Figs. 8 and 10).

7.2 Combination of remote sensing data and models

A profound interpretation of the {H$_2$O,δD} pair distributions is only possible in combination with isotopologue models. In this context and if model data are available, it might be argued that the a posteriori processing is actually not needed because one can compare Type 1 data with model outputs that have been convolved with the Type 1 averaging kernels, thereby simulating the effect of the different H$_2$O and δD kernels. However, model data that have been convolved with Type 1 averaging kernels will be strongly different from the original model data and they will, to a large extent, reflect averaging kernel properties instead of real atmospheric signals (e.g. the slopes of the {H$_2$O,δD} pair distributions will strongly depend on the differences between the Type 1 H$_2$O and δD kernels). It will be difficult to understand what {H$_2$O,δD} pair signals are introduced by the averaging kernels and what {H$_2$O,δD} pair signals are actually modelled. Furthermore, the differences between the Type 1 H$_2$O and δD kernels depend on the atmospheric and geophysical conditions (surface and atmospheric temperatures, atmospheric humidity concentrations, etc.; see, for instance, the example row kernels of the $\mathbf{A}_{11}^*$ and $\mathbf{A}_{22}^*$ matrix blocks in Fig. 12), and since modelled and measured atmospheric state often differ significantly (high small-scale variability of tropospheric humidity), there is a high risk when using inadequate Type 1 H$_2$O and δD kernels when convolving the model data. Under such circumstances it will be very difficult to compare the remote sensing data with the model because the modelled {H$_2$O,δD} pair distributions can be strongly camouflaged by averaging kernels properties.

The different issues with the averaging kernels are less important when using a posteriori processed data because the respective kernels are less complex and have less of an effect on the {H$_2$O,δD} pair distributions (e.g. the slopes of the {H$_2$O,δD} pair distributions are not significantly affected by the kernels). Then the application of the averaging kernel to the model data is less critical and a first-order comparison between modelled and measured {H$_2$O,δD} pair distributions is even possible without applying the averaging kernels to the model (if variations of deep layers are of interest). This possibility becomes evident from Fig. 5. There, the in situ data as depicted in the left panel correspond to point measurements made at 2390 and 3550 m a.s.l., whereas the NDACC/FTIR and MetOp/IASI data reflect the middle troposphere according to their averaging kernels ($\mathbf{A}_{11}^*$ and $\mathbf{A}_{22}^*$ in Figs. 1 and 2). The {H$_2$O,δD} pair distributions of the a posteriori processed NDACC/FTIR and MetOp/IASI data compare well with the in situ data that are not affected by averaging kernels, suggesting that a posteriori processed remote sensing data can be used as a direct reference for a first-order validation of modelled {H$_2$O,δD} pair distributions (there is no need for applying the kernels to the model as long as the dominating {H$_2$O,δD} pair signal of a deep layer is of interest).

A further improved integration of model and remote sensing {H$_2$O,δD} pairs might be achieved by the development of a {H$_2$O,δD} pair remote sensing retrieval simulator (the principle idea of a retrieval simulator is presented in Field et al., 2012).

8 Summary and conclusions

The MUSICA ground- and space-based water vapour isotopologue remote sensing products (generated from NDACC/FTIR and MetOp/IASI spectra with the final MUSICA retrieval version, v2015) are calibrated and their quality is empirically documented. Compared to previous versions, v2015 improves the consistency between the different locations (uniform a priori for all retrievals and improved spectral windows for the NDACC/FTIR retrievals) and the consistency with respect to in situ references (data are calibrated using the aircraft profile references measured between the surface and 7 km altitude during the summer 2013 MUSICA campaign). The remaining bias in the v2015 data is very likely smaller than 15 % and 25 ‰ for the NDACC/FTIR lower tropospheric H$_2$O and δD products, respectively. In the middle troposphere, the remaining bias for the NDACC/FTIR and MetOp/IASI products is estimated to be within 10 % (for H$_2$O) and 15 ‰ (for δD).

Tropospheric δD values are most interesting for science if provided together with H$_2$O, i.e. it is important to validate the {H$_2$O,δD} pair distributions that are obtained

using the remote sensing techniques. MUSICA's surface-based in situ measurements made on Tenerife at 2390 and 3550 m a.s.l. (subtropical North Atlantic) provide a continuous free tropospheric in situ reference record of {H_2O,δD} pairs for validating the remote sensing data. We find that the in situ and the calibrated and a posteriori processed remote sensing products reveal similar {H_2O,δD} pair distributions and consistently capture the three principle moisture pathways to the subtropical free troposphere: transport from the upper troposphere of the extratropics, transport from the lower troposphere over the subtropical/tropical Ocean and uplift via dry convection over the Sahara followed by advection over the Atlantic. We show that the space- and ground-based MUSICA v2015 data are rather consistent on global scale. First, there is no significant bias between both data sets and second, the space- and ground-based products consistently detect extremes in the {H_2O,δD} distribution at different globally distributed locations. This suggests that the calibrations with respect to H_2O and δD reference scales and the validations with respect to the reference {H_2O,δD} pair distributions have global validity.

We present examples of seasonal cycles in the NDACC/FTIR {H_2O,δD} pair distribution and briefly discuss possible links between the seasonality in this distribution and the seasonality in moisture sources and transport processes. Since NDACC/FTIR provides long-term data records, there are good possibilities for studying the {H_2O,δD} pair distributions in a climatological context. In the framework of follow-up studies, it would be interesting to examine whether there is a significant long-term change in the seasonality of the {H_2O,δD} pair distributions at any MUSICA NDACC/FTIR site.

MetOp/IASI offers high horizontal resolution, on a quasi-global scale, and morning as well as evening observations. We present and briefly discuss examples of {H_2O,δD} pair distribution patterns on regional scales as well as on seasonal and diurnal timescales. The regional {H_2O,δD} patterns give insight into the horizontal distribution of humidity control mechanisms; for instance, they suggest regions where humidity is determined mainly by mixing and regions where drying by condensation or moistening by rain re-evaporation is dominant. The diurnal timescale patterns allow conclusions about the mechanisms that drive the diurnal cycle of atmospheric moisture; for instance in the summertime, Sahara dry convection seems to be very important. As soon as more MUSICA MetOp/IASI {H_2O,δD} data are produced, seasonal cycle analyses on global scales could be performed, and specific horizontal {H_2O,δD} patterns for different atmospheric and climate modes (NAO, ENSO, etc.) could be investigated.

The MUSICA {H_2O,δD} pair remote sensing data discussed here are produced from H_2O and δD optimal estimation retrievals by an a posteriori correction method. The a posteriori correction is needed for generating {H_2O,δD} pairs, i.e. H_2O and δD products with the same sensitivities.

MUSICA data are available as a posteriori processed data, and we strongly recommend their usage whenever {H_2O,δD} pair distributions are of interest. At the same time, we advise against using the H_2O and δD optimal estimation products (original retrieval output, not a posteriori processed) for {H_2O,δD} pair distribution studies. The reason is the different sensitivities of H_2O and δD, which imply a significant risk for defective interpretations of {H_2O,δD} pair distributions.

This paper shows that reliable and carefully characterized {H_2O,δD} pair remote sensing observations can be made available by retrievals of spectra measured by NDACC/FTIR instruments and by MetOp/IASI sensors. The data have long-term characteristics and offer global coverage and high resolution (in space and time), thereby opening up new opportunities for addressing the focus research areas that are briefly described in the Introduction section. In the next step, concrete research opportunities should be identified and evaluated. For this purpose, atmospheric models (like COSMO-iso, Pfahl et al., 2012) will be essential. Sensitivity tests with the models are needed in order to reveal the links between different moisture processes and distinct {H_2O,δD} pair distributions and in order to estimate whether the characteristics of the remote sensing data (e.g. their limited sensitivity and vertical resolution) allow the expected {H_2O,δD} pair signals to be detected.

9   Data availability

The MUSICA NDACC/FTIR data are available via the database of NDACC (ftp://ftp.cpc.ncep.noaa.gov/ndacc/MUSICA/) and via ZENODO (Barthlott et al., 2016b). Details are given in Barthlott et al. (2016a).

In the long run, we also plan to disseminate the MUSICA MetOp/IASI data via a database and in a standard data format. At this stage the data are available as ascii data files and can be requested from the MUSICA team (by email to the leading author of this paper). Correct data usage will be assured by direct contact between the data users and the MUSICA team.

The MUSICA aircraft-based and ground-based in situ water vapour isotopologue observations used as the references in this study are discussed in detail in Dyroff et al. (2015) and González et al. (2016), respectively. The data can be requested from the MUSICA team (by email to the leading author of this paper). It is foreseen to provide the data via a dedicated international database at Laboratoire des Science du Climat et de l'Environnement, which is currently in development (see status at https://waterisotopes.lsce.ipsl.fr/).

Appendix A: Milestones of the MUSICA project

MUSICA ends in July 2016. During the last few years, methods for a theoretical characterization and empirical validation of {H$_2$O,δD} pair remote sensing have been developed. The most important milestones and the corresponding publications are collected in Table A1.

Table A1. Important developments/milestones in the context of the MUSICA activities.

Development/milestone	References
Optimal estimation of H$_2$O, HDO and δD	Schneider et al. (2006)
Improving spectroscopic line parameterization using atmospheric spectra	Schneider and Hase (2009); Schneider et al. (2011)
The MUSICA FTIR/NDACC retrieval, H$_2$O and δD proxies	Schneider et al. (2012); Barthlott et al. (2016a)
A posteriori processing for generating optimal {H$_2$O,δD} pairs	Schneider et al. (2012)
The MUSICA MetOp/IASI retrieval	Schneider and Hase (2011); Wiegele et al. (2014)
Validation of {H$_2$O,δD} pairs	Wiegele et al. (2014); Schneider et al. (2015)
Using XCO$_2$ for quality filtering of MUSICA NDACC/FTIR	Barthlott et al. (2015)
In situ profile references (ISOWAT aircraft campaign, 0–7 km)	Dyroff et al. (2015); Schneider et al. (2015)
Continuous in situ reference for the free troposphere	González et al. (2016)

Appendix B: MUSICA in the context of other isotopologue ratio remote sensing data sets

We would like to remark that the results as shown in this paper are only valid for the MUSICA products. This appendix gives a brief overview on other (non-MUSICA) tropospheric water vapour isotopologue remote sensing products and briefly discusses their differences to the MUSICA products.

B1 The TCCON XH$_2$O and XHDO data

The ground-based FTIR water vapour isotopologue products that are made available via TCCON (www.tccon.caltech.edu/) are fundamentally different from the MUSICA ground-based FTIR isotopologue products.

A TCCON-like product is discussed in Rokotyan et al. (2014). It relies on near-infrared absorption lines (where $HD^{16}O$ is a rather weak absorber) and the isotopologue ratios are calculated a posteriori from independently retrieved $H_2^{16}O$ and $HD^{16}O$ column amounts. Such a posteriori calculated ratios are affected by the different sensitivities of the individual $H_2^{16}O$ and $HD^{16}O$ retrievals. At the moment, the TCCON kernels do not give information about the cross-correlations between the $H_2^{16}O$ and $HD^{16}O$ product, and it is not possible to calculate kernels for humidity and δD proxies. This means that no Type 2 product can be calculated. The TCCON retrievals use NCEP (National Centers for Environmental Prediction) humidity analyses as H_2O a priori and construct the δD a priori profiles by assuming a fixed linear correlation between ln[H_2O] and δD ($\delta D = 0.0695 \times$ ln[H_2O] $+ 0.28$).

B2 Satellite-based tropospheric water vapour isotopologue data

A brief overview of available products of tropospheric water vapour isotopologues and the respective satellite sensors is given in the Tables B1 and B2.

The thermal nadir sensors TES and IASI have the best sensitivity with respect to the water vapour isotopologues in the middle troposphere (about 2–8 km altitude). In addition to the MUSICA research team, a group at the University of Brussels (ULB) is working on IASI water vapour isotopologue retrievals. The ULB IASI retrieval uses two small spectral microwindows (1193–1223 and 1251–1253 cm^{-1}) and fits the proxies for humidity, δD and CH$_4$ below 10 km altitude as well as ground temperature (Lacour et al., 2012). It uses the EUMETSAT Level 2 temperature output for the whole atmosphere and the EUMETSAT Level 2 humidity output for altitudes above 10 km (no fit). The ULB group uses the same globally uniform a priori data as the MUSICA group. For the ULB retrieval, Type 2 products (a posteriori processed, H_2O and δD have almost identical sensitivities)

and Type 1 products (individual optimal estimation of H_2O and δD) can be made available.

Another tropospheric isotopologue product is generated from AURA/TES spectra. It has first been presented by Worden et al. (2006), whereby small spectral microwindows have been fitted (similar to the ULB IASI retrieval). The TES version 5 product used nowadays is discussed in Worden et al. (2012), and the respective retrieval set-up is rather similar to the MUSICA IASI retrieval set-up: a broad spectral window, simultaneous fit of proxies for humidity and δD as well as of temperature and the interfering gases throughout the atmosphere. However, for the TES retrieval the H_2O a priori assumption comes from the NCEP humidity analyses, and the δD a priori has a latitudinal dependency. The generation of a Type 2 product is theoretically possible, but it is currently not provided. TES measures limb and thermal nadir spectra (the isotopologue data are generated from the nadir spectra). It has a similar spectral coverage to IASI, but a significantly higher spectral resolution and, on the other hand, much sparser daily horizontal coverage. Lacour et al. (2015) showed a cross-validation of the TES version 5 products and the IASI products generated by the ULB group.

Space-based sensors measuring solar short-wave infrared spectra (SWIR) reflected on the Earth's surface theoretically have better sensitivity in the lower troposphere than the thermal nadir sensors. Retrievals using the sensors SCIAMACHY and GOSAT have been presented and assessed by Frankenberg et al. (2009), Frankenberg et al. (2013), Boesch et al. (2013) and Scheepmaker et al. (2015). All use humidity analyses (NCEP or ECMWF) as humidity a priori, but a globally uniform δD a priori. The respective retrievals work independently for the different isotopologues, and the isotopologue ratio is calculated after the retrieval process. This is an important difference to the thermal nadir retrievals, which optimally estimate the proxies of H_2O and HDO / H_2O. The near-infrared retrievals are thus affected by the different sensitivities for the different isotopologues. A further difference is that in the near-infrared, the absorption signatures of the secondary isotopologue ($HD^{16}O$) is significantly smaller than in the thermal infrared. The daily horizontal coverage of these sensors is much sparser than for IASI. For the current SWIR retrievals, no humidity and δD proxy kernels are available, and it is not possible to assess the difference between the H_2O and δD kernels and to correct for it; i.e. it is not possible to perform an a posteriori correction and generate a Type 2 product.

Table B1. Overview of tropospheric water vapour isotopologue retrievals using space-based observations.

Research group/sensor	Spectral window	Fitted parameter	References and remarks
MUSICA (IMK-ASF)/IASI	1190–1400 cm^{-1}	$(\ln[H_2O] + \ln[HDO])/2$ $\ln[HDO] - \ln[H_2O]$ CH_4, N_2O, CO_2 and HNO_3 atmospheric temperature ground temperature	Schneider and Hase (2011), Wiegele et al. (2014), atm. temp. constrained to EUMETSAT L2, only clear sky retrievals
ULB (U. Brussels)/IASI	1193–1223 cm^{-1} 1251–1253 cm^{-1}	$(\ln[H_2O] + \ln[HDO])/2$ $\ln[HDO] - \ln[H_2O]$ CH_4 ground temperature	Lacour et al. (2012), Lacour et al. (2015) only fit for 0–10 km, atm. temp. from EUMETSAT L2, only clear sky retrievals
NASA/TES	1170–1320 cm^{-1}	$(\ln[H_2O] + \ln[HDO])/2$ $\ln[HDO] - \ln[H_2O]$ CH_4 and N_2O atmospheric temperature ground temperature cloud (τ and pressure)	Worden et al. (2006), Worden et al. (2012)
SRON/SCIAMACHY	4212–4248 cm^{-1}	$H_2^{16}O$, $H_2^{18}O$ and $HD^{16}O$ CH_4 and CO	Frankenberg et al. (2009), Scheepmaker et al. (2015)
NASA/GOSAT	6311–6441 cm^{-1}	H_2O and HDO	Frankenberg et al. (2013)
U. Leicester/GOSAT	6439–6464 cm^{-1}	H_2O and HDO	Boesch et al. (2013), uses CH_4 obtained from extra CH_4 retrieval

Table B2. Space-based sensors with available tropospheric water vapour isotopologue retrieval products.

| Sensor	Meas. geo.	Pixel size	Meas. per day	Temporal coverage	Spectral res.
IASI	thermal nadir	12 km diameter (at nadir)	$\approx$ 1.3 million	IASI-A: since 2007 IASI-B: since 2013 IASI-C: scheduled for 2018	0.5 cm^{-1}
TES	thermal nadir	5×8 km (at nadir)	$\approx$ 2100	since 2002 (since 2010 temporarily)	0.1 cm^{-1}
SCIAMACHY	SWIR	120×30 km	$\approx$ 32 000	2003–2012 (after 2007 increased detector degradation)	$\approx$ 0.45 cm^{-1}
GOSAT	SWIR	10 km diameter	$\approx$ 10 000	since 2009	0.4 cm^{-1}

Appendix C: Reference profiles

C1 Coincidences in space and time

During July 2013 we performed an aircraft campaign in the surroundings of Tenerife. We operated the ISOWAT instrument (Dyroff et al., 2010) aboard the aircraft and measured highly resolved vertical profiles of H$_2$O and δD from sea surface up to almost 7 km altitude on 6 individual days (21 Jul 2013, 22 Jul 2013, 24 Jul 2013, 25 Jul 2013, 30 Jul 2013 and 31 Jul 2013; Dyroff et al., 2015; Schneider et al., 2015). The aircraft's ascent and descent took place between 10:30 and 13:30 UT. Figure C1 shows a site map indicating the horizontal flight track of the aircraft (grey line) as well as the location of the Tenerife FTIR instrument (green star) and the IASI observation pixels (coloured squares and diamonds).

A main characteristic of tropospheric humidity is the high short-term and small-scale variability, which make intercomparison studies difficult. Concerning temporal variability, Steinke et al. (2015) reported good correlation of integrated water vapour (IWV) observations and simulations made within 3 h (see their Fig. 7). Vogelmann et al. (2015) use DIAL (differential absorption lidar) for estimating temporal mismatches in vertical profiles. Their Fig. 6 reports middle tropospheric (4–6 km) H$_2$O variabilities within 2 h of about 20 % and within 1 h of about 15 %. This variability increases strongly in the upper troposphere where they found about 60 % within 2 h. When interpreting that study, we have to take into account that the DIAL detects vertically high-resolution profiles, whereas the FTIR and IASI remote sensing data represent deep layers (where variability largely cancels out). Spatial variability can be estimated by space-based observations or by models. Steinke et al. (2015) used ICON simulations and estimated the scatter for humidity encountered at a distance of 10 km to be about 4 % (right column in their Fig. 4 using an IWV of 12 kg m^{-2} from their Fig. 2). In Wiegele et al. (2014), we estimated a variability of about 19 % and 17 ‰ for middle tropospheric H$_2$O and δD measured within an 110 km × 110 km area around Tenerife, whereby at least half of this variability is due to the random errors in the IASI data.

The temporal and spatial variability of humidity fields in the surroundings of Tenerife has been estimated in different studies (Schneider et al., 2010a, b; Wiegele et al., 2014; González et al., 2016) using NDACC/FTIR, MetOp/IASI, ground-based in situ, radiosondes, GPS, radiometers and sun photometer data. Observations made for the middle troposphere within 2 h have a scatter of typically 10 % (for H$_2$O) and 10 ‰ (for δD) that cannot be explained by uncertainties of the instruments. However, close to the surface at the Izaña Observatory, the variability is larger and shows a strong diurnal cycle (Schneider et al., 2010b; González et al., 2016), which is caused by local circulation (thermal upslope flow reaches the island's mountains in the late morning hours). These local circulations have to be considered when compar-
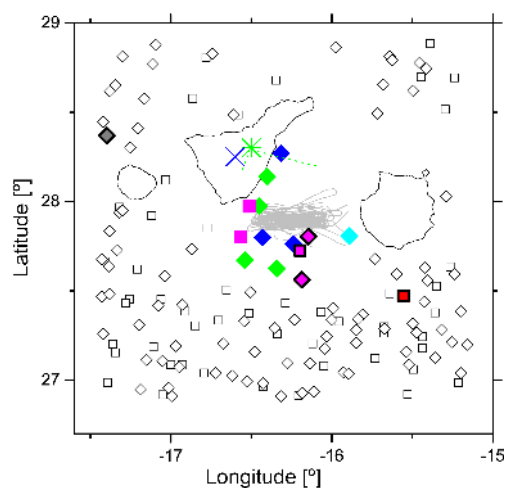
Figure C1. Site map indicating the location of the different instruments and ground pixels during the aircraft campaign on 6 days in July 2013. Green star: Izaña Observatory (location of the first Picarro and the FTIR; the green dashed lines indicate the line of sight of the FTIR between 08:15 and 13:30 UT); blue star: Teide Observatory (location of the second Picarro); grey lines: aircraft flight track during ISOWAT measurements; black squares and diamonds: cloud-free ground pixels of IASI-A and IASI-B, respectively, during the six aircraft flights; red filled squares and diamonds: pixels that fulfil our coincidence criteria for IASI-A and IASI-B, respectively, whereby the different filling colour corresponds to the 6 different days as in Figs. 3 and 4.

ing measurements made in Izaña with measurements made at the free tropospheric location of the aircraft. Since the H$_2$O and δD signals as measured in Izaña in the later morning are already strongly affected by the upslope airflow that is developing during the late morning, early morning data are better representative of the free troposphere. For this reason, we compare FTIR data measured between 08:15 UT and 09:45 UT (for July this means solar elevation between 25 and 45°, which is about 2 and 3.5 h after sunrise) with the free tropospheric aircraft measurements made between 10:30 and 13:30 UT (see Fig. 3 in Sect. 3). This means that there is a temporal mismatch between the FTIR and the ISOWAT observations between 45 min and 5 h for the measurement pairs we define as optimal coincidences. This increases the mismatch uncertainty by about a factor of 3, i.e. from 10 % and 10 ‰ to 30 % and 30 ‰ (this estimatiuon is based on Fig. 12 of Schneider et al., 2010b). Nevertheless, this is what we define as optimal coincidences.

Figure C2 shows the same as Fig. 3, but for FTIR data that have been measured during the time of the aircraft profile measurements, i.e. in the late morning hours and during midday. The comparison plots show relatively large variability in FTIR data that represent the atmospheric layer just above the island, revealing the large impact of the local diurnal upslope flow on the FTIR observations. Although for this comparison the temporal mismatches are rather low, it does not represent
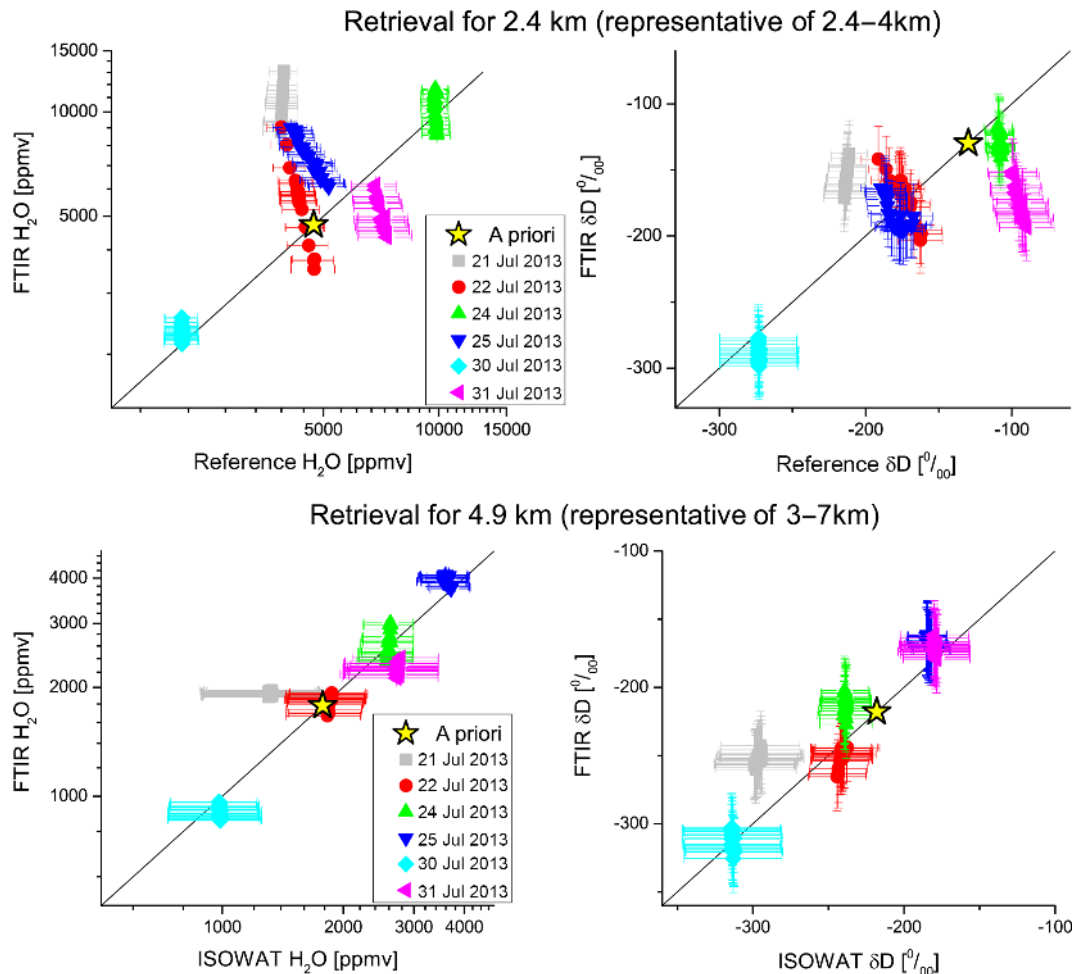
Figure C2. Same as Fig. 3, but for FTIR measurements corresponding to best temporal coincidences (FTIR observations made during the 3 h of the aircraft flights, typically 10:30–13:30 UT).

optimal coincidences because the strong local upslope flow on the island means that the FTIR and the ISOWAT instrument detect different air masses.

The coloured squares and diamonds in Fig. C1 indicate the locations of the IASI observation pixels, whereby the different colours correspond to the different days (see legend in Fig. 4). We require, as coincidence criteria, that the observation pixel is not further away than 50 km from the aircraft's track (coloured squares and diamonds group around the track, which is indicated as the grey line). On the 2 days 21 Jul 2013 and 22 Jul 2013 there are no IASI pixels within 50 km of the aircraft's track and for those days we also include observation pixels that are located more than 100 km away from the flight track. These are the grey and red pixels marked by a black edge, indicating that they correspond to non-optimal coincidences. In addition, there are three magenta-coloured pixels (representing day 31 Jul 2013) that are marked by black edges. These are also representative of non-optimal coincidences, since on day 31 July 2013 there

was a very sharp gradient from the southeast of the flight track (air mass with strong SAL conditions) to the northwest of the flight track (air mass with weaker SAL conditions), and the aircraft's ISOWAT measurements and IASI detect air masses of different characteristics (for a more detailed discussion of this day, 31 Jul 2013, please see Appendix A of Schneider et al., 2015).

C2 Ceiling altitude and uncertainties

The reference profiles are constructed from the ISOWAT measurements (surface up to almost 7 km) and climatological values assumed above the ceiling altitude (see Sect. 2.5). This profile (ISOWAT + climatology) is then smoothed by the averaging kernel of the remote sensor. The uncertainty of ISOWAT is 4 % for H$_2$O and typically better than 10 ‰ for δD (it can only reach high values for rather dry air, e.g. 35 ‰ when the H$_2$O concentration is below 500 ppm, Dyroff et al., 2015). However, above the ceiling altitude we have no measurements and the uncertainty is significantly

larger. We assume 100 % and 80 ‰ for H_2O and δD, respectively. These large uncertainties for the atmosphere above the ceiling altitude propagate to lower altitudes due to the smoothing with the averaging kernels (see typical row kernels in Figs. 1 and 2). In fact, the error bars on the smoothed reference data for 4.9 km as well as for 2.4 km as depicted in Figs. 3, 4 and C2 are dominated by unavailable reference H_2O and δD values above 6–7 km (the δD error bars are only dominated by the uncertainty in the δD measurements up to 7 km for very dry conditions).

For the references used for the FTIR data validation at 2.4 km altitude (top panels of Figs. 3 and C2), the uncertainty introduced from missing data above the ceiling altitude can reach 15 % for H_2O and 12 ‰ for δD. For the FTIR data validation at 4.9 km altitude (bottom panels of Figs. 3 and C2), the respective uncertainty can reach 25 % for H_2O and 20 ‰ for δD. For the IASI data validation at 4.9 km, the respective uncertainties are 25–6 % for H_2O and 20–5 ‰ for δD. The values depend on both the averaging kernels as well as the ceiling altitude (e.g. on 21 Jul 2013 we only reached 6.0 km, leading to higher uncertainties than for days when we reached 6.8 km). Please consider that the kernels in Figs. 1 and 2 are on a logarithmic scale; i.e. a value of 0.1 of the 4.9 km row kernel at 6.5 km altitude together with a profile uncertainty of 80 ‰ (no measurement at 6.5 km) means an uncertainty in the smoothed profile value at 4.9 km of 8 ‰. The error sums up to 15 ‰ by adding up the contributions from all altitudes above 6.5 km.

For the validation/calibration of the remote sensing data, it is essential to have reference measurements that cover the troposphere from the surface up to high altitudes. During the ISOWAT campaign we almost reached 7 km during most of the flights and we are not aware of another δD reference profile data set with similarly good altitude coverage.

References

Barthlott, S., Schneider, M., Hase, F., Wiegele, A., Christner, E., González, Y., Blumenstock, T., Dohe, S., García, O. E., Sepúlveda, E., Strong, K., Mendonca, J., Weaver, D., Palm, M., Deutscher, N. M., Warneke, T., Notholt, J., Lejeune, B., Mahieu, E., Jones, N., Griffith, D. W. T., Velazco, V. A., Smale, D., Robinson, J., Kivi, R., Heikkinen, P., and Raffalski, U.: Using XCO$_2$ retrievals for assessing the long-term consistency of NDACC/FTIR data sets, Atmos. Meas. Tech., 8, 1555–1573, doi:10.5194/amt-8-1555-2015, 2015.

Barthlott, S., Schneider, M., Hase, F., Blumenstock, T., Kiel, M., Dubravica, D., García, O. E., Sepúlveda, E., Mengistu Tsidu, G., Takele Kenea, S., Grutter, M., Plaza, E. F., Stremme, W., Strong, K., Weaver, D., Palm, M., Warneke, T., Notholt, J., Mahieu, E., Servais, C., Jones, N., Griffith, D. W. T., Smale, D., and Robinson, J.: Tropospheric water vapour isotopologue data (H$_2^{16}$O, H$_2^{18}$O and HD^{16}O) as obtained from NDACC/FTIR solar absorption spectra, Earth Syst. Sci. Data Discuss., doi:10.5194/essd-2016-9, in review, 2016a.

Barthlott, S., Schneider, M., Hase, F., Blumenstock, T., Mengistu Tsidu, G., Grutter de la Mora, M., Strong, K., Notholt, J., Mahieu, E., Jones, N., and Smale, D.: The ground-based MUSICA dataset: Tropospheric water vapour isotopologues (H$_2^{16}$O, H$_2^{18}$O and HD^{16}O) as obtained from NDACC/FTIR solar absorption spectra, doi:10.5281/zenodo.48902, 2016b.

Berkelhammer, M., Risi, C., Kurita, N., and Noone, D. C.: The moisture source sequence for the Madden-Julian Oscillation as derived from satellite retrievals of HDO and H$_2$O, J. Geophys. Res.-Atmos., 117, D03106, doi:10.1029/2011JD016803, 2012.

Boesch, H., Deutscher, N. M., Warneke, T., Byckling, K., Cogan, A. J., Griffith, D. W. T., Notholt, J., Parker, R. J., and Wang, Z.: HDO/H$_2$O ratio retrievals from GOSAT, Atmos. Meas. Tech., 6, 599–612, doi:10.5194/amt-6-599-2013, 2013.

Dansgaard, W.: Stable isotopes in precipitation, Tellus, 16, 436–468, doi:10.1111/j.2153-3490.1964.tb00181.x, 1964.

Dyroff, C., Fütterer, D., and Zahn, A.: Compact diode-laser spectrometer ISOWAT for highly sensitive airborne measurements of water-isotope ratios, Appl. Phys. B, 98, 537–548, doi:10.1007/s00340-009-3775-6, 2010.

Dyroff, C., Sanati, S., Christner, E., Zahn, A., Balzer, M., Bouquet, H., McManus, J. B., González-Ramos, Y., and Schneider, M.: Airborne in situ vertical profiling of HDO / H$_2^{16}$O in the subtropical troposphere during the MUSICA remote sensing validation campaign, Atmos. Meas. Tech., 8, 2037–2049, doi:10.5194/amt-8-2037-2015, 2015.

Field, R. D., Risi, C., Schmidt, G. A., Worden, J., Voulgarakis, A., LeGrande, A. N., Sobel, A. H., and Healy, R. J.: A Tropospheric Emission Spectrometer HDO/H$_2$O retrieval simulator for climate models, Atmos. Chem. Phys., 12, 10485–10504, doi:10.5194/acp-12-10485-2012, 2012.

Field, R. D., Kim, D., LeGrande, A. N., Worden, J., Kelley, M., and Schmidt, G. A.: Evaluating climate model performance in the tropics with retrievals of water isotopic composition from Aura TES, Geophys. Res. Lett., 41, 6030–6036, doi:10.1002/2014GL060572, 2014.

Frankenberg, C., Yoshimura, K., Warneke, T., Aben, I., Butz, A., Deutscher, N., Griffith, D., Hase, F., Notholt, J., Schneider, M., Schrejver, H., and Röckmann, T.: Dynamic processes governing lower-tropospheric HDO/H_2O ratios as observed from space and ground, Science, 325, 1374–1377, doi:10.1126/science.1173791, 2009.

Frankenberg, C., Wunch, D., Toon, G., Risi, C., Scheepmaker, R., Lee, J.-E., Wennberg, P., and Worden, J.: Water vapor isotopologue retrievals from high-resolution GOSAT shortwave infrared spectra, Atmos. Meas. Tech., 6, 263–274, doi:10.5194/amt-6-263-2013, 2013.

Galewsky, J., Sobel, A., and Held, I.: Diagnosis of Subtropical Humidity Dynamics Using Tracers of Last Saturation, J. Atmos. Sci., 62, 3353–3367, 2005.

Gat, J. R.: Atmospheric water balance – the isotopic perspective, Hydrol. Process., 14, 1357–1369, doi:10.1002/1099-1085(20000615)14:8<1357::AID-HYP986>3.0.CO;2-7, 2000.

Gisi, M., Hase, F., Dohe, S., and Blumenstock, T.: Camtracker: a new camera controlled high precision solar tracker system for FTIR-spectrometers, Atmos. Meas. Tech., 4, 47–54, doi:10.5194/amt-4-47-2011, 2011.

González, Y., Schneider, M., Dyroff, C., Rodríguez, S., Christner, E., García, O. E., Cuevas, E., Bustos, J. J., Ramos, R., Guirado-Fuentes, C., Barthlott, S., Wiegele, A., and Sepúlveda, E.: Detecting moisture transport pathways to the subtropical North Atlantic free troposphere using paired H_2O-δD in situ measurements, Atmos. Chem. Phys., 16, 4251–4269, doi:10.5194/acp-16-4251-2016, 2016.

Hase, F., Hannigan, J. W., Coffey, M. T., Goldman, A., Höpfner, M., Jones, N. B., Rinsland, C. P., and Wood, S.: Intercomparison of retrieval codes used for the analysis of high-resolution, J. Quant. Spectrosc. Ra., 87, 25–52, 2004.

Herman, R. L., Cherry, J. E., Young, J., Welker, J. M., Noone, D., Kulawik, S. S., and Worden, J.: Aircraft validation of Aura Tropospheric Emission Spectrometer retrievals of HDO / H_2O, Atmos. Meas. Tech., 7, 3127–3138, doi:10.5194/amt-7-3127-2014, 2014.

International in situ water isotope database: available at: https://waterisotopes.lsce.ipsl.fr, 2013.

Kuang, Z., Toon, G., Wennberg, P., and Yung, Y.: Measured HDO/H_2O ratios across the tropical tropopause, Geophys. Res. Lett., 30, 251–254, doi:10.1029/2003GL017023, 2003.

Lacour, J.-L., Risi, C., Clarisse, L., Bony, S., Hurtmans, D., Clerbaux, C., and Coheur, P.-F.: Mid-tropospheric δD observations from IASI/MetOp at high spatial and temporal resolution, Atmos. Chem. Phys., 12, 10817–10832, doi:10.5194/acp-12-10817-2012, 2012.

Lacour, J.-L., Clarisse, L., Worden, J., Schneider, M., Barthlott, S., Hase, F., Risi, C., Clerbaux, C., Hurtmans, D., and Coheur, P.-F.: Cross-validation of IASI/MetOp derived tropospheric δD with TES and ground-based FTIR observations, Atmos. Meas. Tech., 8, 1447–1466, doi:10.5194/amt-8-1447-2015, 2015.

Marsham, J. H., Dixon, N. S., Garcia-Carreras, L., Lister, G. M. S., Parker, D. J., Knippertz, P., and Birch, C. E.: The role of moist convection in the West African monsoon system: Insights from continental-scale convection-permitting simulations, Geophys. Res. Lett., 40, 1843–1849, doi:10.1002/grl.50347, 2013.

Noone, D.: Pairing Measurements of the Water Vapor Isotope Ratio with Humidity to Deduce Atmospheric Moistening and Dehydra-

tion in the Tropical Midtroposphere, J. Climate, 25, 4476–4494, doi:10.1175/JCLI-D-11-00582.1, 2012.

NDACC database: available at: ftp://ftp.cpc.ncep.noaa.gov/ndacc/MUSICA/, 2016.

Ortega, P., Lehner, F., Swingedouw, D., Masson-Delmotte, V., Raible, C. C., Casado, M., and Yiou, P.: A model-tested North Atlantic Oscillation reconstruction for the last millennium, Nature, 523, 71–74, doi:10.1038/nature14518, 2015.

Pfahl, S., Wernli, H., and Yoshimura, K.: The isotopic composition of precipitation from a winter storm – a case study with the limited-area model COSMOiso, Atmos. Chem. Phys., 12, 1629–1648, doi:10.5194/acp-12-1629-2012, 2012.

Risi, C., Noone, D., Worden, J., Frankenberg, C., Stiller, G., Kiefer, M., Funke, B., Walker, K., Bernath, P., Schneider, M., Bony, S., Lee, J., Brown, D., and Sturm, C.: Process-evaluation of tropospheric humidity simulated by general circulation models using water vapor isotopic observations. Part 2: an isotopic diagnostic to understand the mid and upper tropospheric moist bias in the tropics and subtropics, J. Geophys. Res., 117, D05304, doi:10.1029/2011JD016623, 2012a.

Risi, C., Noone, D., Worden, J., Frankenberg, C., Stiller, G., Kiefer, M., Funke, B., Walker, K., Bernath, P., Schneider, M., Wunch, D., Sherlock, V., Deutscher, N., Griffith, D., Wennberg, P., Strong, K., Barthlott, S., Hase, F., G. O., Smale, D., Mahieu, E., Sayres, D., Bony, S., Lee, J., Brown, D., Uemura, R., and Sturm, C.: Process-evaluation of tropospheric humidity simulated by general circulation models using water vapor isotopic observations. Part 1: comparison between models and datasets, J. Geophys. Res., 117, D05303, doi:10.1029/2011JD016621, 2012b.

Rodríguez, S., Alastuey, A., Alonso-Pérez, S., Querol, X., Cuevas, E., Abreu-Afonso, J., Viana, M., Pérez, N., Pandolfi, M., and de la Rosa, J.: Transport of desert dust mixed with North African industrial pollutants in the subtropical Saharan Air Layer, Atmos. Chem. Phys., 11, 6663–6685, doi:10.5194/acp-11-6663-2011, 2011.

Rokotyan, N. V., Zakharov, V. I., Gribanov, K. G., Schneider, M., Bréon, F.-M., Jouzel, J., Imasu, R., Werner, M., Butzin, M., Petri, C., Warneke, T., and Notholt, J.: A posteriori calculation of $\delta^{18}O$ and δD in atmospheric water vapour from ground-based near-infrared FTIR retrievals of $H_2^{16}O$, $H_2^{18}O$, and $HD^{16}O$, Atmos. Meas. Tech., 7, 2567–2580, doi:10.5194/amt-7-2567-2014, 2014.

Rothman, L. S., Gordon, I. E., Barbe, A., Chris Benner, D., Bernath, P. F., Birk, M., Boudon, V., Brown, L. R., Campargue, A., Champion, J.-P., Chance, K., Coudert, L. H., Dana, V., Devi, V. M., Fally, S., Flaud, J.-M., Gamache, R. R., Goldman, A., Jacquemart, D., Kleiner, I., Lacome, N., Lafferty, W. J., Mandin, J.-Y., Massie, S. T., Mikhailenko, S. N., Miller, C. E., Moazzen-Ahmadi, N., Naumenko, O. V., Nikitin, A. V., Orphal, J., Perevalov, V. I., Perrin, A., Predoi-Cross, A., Rinsland, C. P., Rotger, M., Simecková, M., Smith, M. A. H., Sung, K., Tashkun, S. A., Tennyson, J., Toth, R. A., Vandaele, A. C., and Vander-Auwera, J.: The HITRAN 2008 molecular spectroscopic database, J. Quant. Spectrosc. Ra., 110, 533–572, doi:10.1016/j.jqsrt.2009.02.013, 2009.

Rothman, L., Gordon, I., Babikov, Y., Barbe, A., Benner, D. C., Bernath, P., Birk, M., Bizzocchi, L., Boudon, V., Brown, L., Campargue, A., Chance, K., Cohen, E., Coudert, L., Devi, V., Drouin, B., Fayt, A., Flaud, J.-M., Gamache, R., Harrison, J.,

Hartmann, J.-M., Hill, C., Hodges, J., Jacquemart, D., Jolly, A., Lamouroux, J., Roy, R. L., Li, G., Long, D., Lyulin, O., Mackie, C., Massie, S., Mikhailenko, S., Müller, H., Naumenko, O., Nikitin, A., Orphal, J., Perevalov, V., Perrin, A., Polovtseva, E., Richard, C., Smith, M., Starikova, E., Sung, K., Tashkun, S., Tennyson, J., Toon, G., Tyuterev, V., and Wagner, G.: The HITRAN2012 molecular spectroscopic database, J. Quant. Spectrosc. Ra., 130, 4–50, doi:10.1016/j.jqsrt.2013.07.002, 2013.

Scheepmaker, R. A., Frankenberg, C., Deutscher, N. M., Schneider, M., Barthlott, S., Blumenstock, T., Garcia, O. E., Hase, F., Jones, N., Mahieu, E., Notholt, J., Velazco, V., Landgraf, J., and Aben, I.: Validation of SCIAMACHY HDO/H_2O measurements using the TCCON and NDACC-MUSICA networks, Atmos. Meas. Tech., 8, 1799–1818, doi:10.5194/amt-8-1799-2015, 2015.

Schneider, M. and Hase, F.: Improving spectroscopic line parameters by means of atmospheric spectra: Theory and example for water vapour and solar absorption spectra, J. Quant. Spectrosc. Ra., 110, 1825–1839, doi:10.1016/j.jqsrt.2009.04.011, 2009.

Schneider, M. and Hase, F.: Optimal estimation of tropospheric H_2O and δD with IASI/METOP, Atmos. Chem. Phys., 11, 11207–11220, doi:10.5194/acp-11-11207-2011, 2011.

Schneider, M., Hase, F., Blavier, J.-F., Toon, G. C., and Leblanc, T.: An empirical study on the importance of a speed-dependent Voigt line shape model for tropospheric water vapor profile remote sensing, J. Quant. Spectrosc. Ra., 112, 465–474, doi:10.1016/j.jqsrt.2010.09.008, 2011.

Schneider, M., Hase, F., and Blumenstock, T.: Ground-based remote sensing of HDO/H_2O ratio profiles: introduction and validation of an innovative retrieval approach, Atmos. Chem. Phys., 6, 4705–4722, doi:10.5194/acp-6-4705-2006, 2006.

Schneider, M., Romero, P. M., Hase, F., Blumenstock, T., Cuevas, E., and Ramos, R.: Continuous quality assessment of atmospheric water vapour measurement techniques: FTIR, Cimel, MFRSR, GPS, and Vaisala RS92, Atmos. Meas. Tech., 3, 323–338, doi:10.5194/amt-3-323-2010, 2010a.

Schneider, M., Sepúlveda, E., García, O., Hase, F., and Blumenstock, T.: Remote sensing of water vapour profiles in the framework of the Total Carbon Column Observing Network (TCCON), Atmos. Meas. Tech., 3, 1785–1795, doi:10.5194/amt-3-1785-2010, 2010b.

Schneider, M., Barthlott, S., Hase, F., González, Y., Yoshimura, K., García, O. E., Sepúlveda, E., Gomez-Pelaez, A., Gisi, M., Kohlhepp, R., Dohe, S., Blumenstock, T., Wiegele, A., Christner, E., Strong, K., Weaver, D., Palm, M., Deutscher, N. M., Warneke, T., Notholt, J., Lejeune, B., Demoulin, P., Jones, N., Griffith, D. W. T., Smale, D., and Robinson, J.: Ground-based remote sensing of tropospheric water vapour isotopologues within the project MUSICA, Atmos. Meas. Tech., 5, 3007–3027, doi:10.5194/amt-5-3007-2012, 2012.

Schneider, M., González, Y., Dyroff, C., Christner, E., Wiegele, A., Barthlott, S., García, O. E., Sepúlveda, E., Hase, F., Andrey, J., Blumenstock, T., Guirado, C., Ramos, R., and Rodríguez, S.: Empirical validation and proof of added value of MUSICA's tropospheric δD remote sensing products, Atmos. Meas. Tech., 8, 483–503, doi:10.5194/amt-8-483-2015, 2015.

Sherwood, S. C., Bony, S., and Dufresne, J.-L.: Spread in model climate sensitivity traced to atmospheric convective mixing, Nature, 505, 37–42, doi:10.1038/nature12829, 2014.

Steinke, S., Eikenberg, S., Löhnert, U., Dick, G., Klocke, D., Di Girolamo, P., and Crewell, S.: Assessment of small-scale integrated water vapour variability during HOPE, Atmos. Chem. Phys., 15, 2675–2692, doi:10.5194/acp-15-2675-2015, 2015.

Steinwagner, J., Fueglistaler, S., Stiller, G. P., von Clarmann, T., Kiefer, M., Borsboom, P.-P., van Delden, A., and Röckmann, T.: Tropical dehydration processes constrained by the seasonality of stratospheric deuterated water, Nature Geoscience, 3, 262–266, doi:10.1038/ngeo822, 2010.

Stevens, B. and Bony, S.: What Are Climate Models Missing?, Science, 340, 1053–1054, doi:10.1126/science.1237554, 2013.

Sutanto, S. J., Hoffmann, G., Scheepmaker, R. A., Worden, J., Houweling, S., Yoshimura, K., Aben, I., and Röckmann, T.: Global-scale remote sensing of water isotopologues in the troposphere: representation of first-order isotope effects, Atmos. Meas. Tech., 8, 999–1019, doi:10.5194/amt-8-999-2015, 2015.

Tuinenburg, O. A., Risi, C., Lacour, J. L., Schneider, M., Wiegele, A., Worden, J., Kurita, N., Duvel, J. P., Deutscher, N., Bony, S., Coheur, P. F., and Clerbaux, C.: Moist processes during MJO events as diagnosed from water isotopic measurements from the IASI satellite, J. Geophys. Res.-Atmos., 120, 10619–10636, doi:10.1002/2015JD023461, 2015.

Vogelmann, H., Sussmann, R., Trickl, T., and Reichert, A.: Spatiotemporal variability of water vapor investigated using lidar and FTIR vertical soundings above the Zugspitze, Atmos. Chem. Phys., 15, 3135–3148, doi:10.5194/acp-15-3135-2015, 2015.

Wiegele, A., Schneider, M., Hase, F., Barthlott, S., García, O. E., Sepúlveda, E., González, Y., Blumenstock, T., Raffalski, U., Gisi, M., and Kohlhepp, R.: The MUSICA MetOp/IASI H_2O and δD products: characterisation and long-term comparison to NDACC/FTIR data, Atmos. Meas. Tech., 7, 2719–2732, doi:10.5194/amt-7-2719-2014, 2014.

Worden, J. R., Bowman, K., Noone, D., Beer, R., Clough, S., Eldering, A., Fisher, B., Goldman, A., Gunson, M., Herman, R., Kulawik, S. S., Lampel, M., Luo, M., Osterman, G., Rinsland, C., Rodgers, C., Sander, S., Shephard, M., and Worden, H.: TES observations of the tropospheric HDO/H_2O ratio: retrieval approach and characterization, J. Geophys. Res., 11, D16309, doi:10.1029/2005JD006606, 2006.

Worden, J., Noone, D., Bowman, K., Beer, R., Eldering, A., Fisher, B., Gunson, M., Goldman, A., Herman, R., Kulawik, S. S., Lampel, M., Osterman, G., Rinsland, C., Rodgers, C., Sander, S., Shephard, M., Webster, R., and Worden, H.: Importance of rain evaporation and continental convection in the tropical water cycle, Nature, 445, 528–532, doi:10.1038/nature05508, 2007.

Worden, J., Noone, D., Galewsky, J., Bailey, A., Bowman, K., Brown, D., Hurley, J., Kulawik, S., Lee, J., and Strong, M.: Estimate of bias in Aura TES HDO/H_2O profiles from comparison of TES and in situ HDO/H_2O measurements at the Mauna Loa observatory, Atmos. Chem. Phys., 11, 4491–4503, doi:10.5194/acp-11-4491-2011, 2011.

Worden, J., Kulawik, S., Frankenberg, C., Payne, V., Bowman, K., Cady-Peirara, K., Wecht, K., Lee, J.-E., and Noone, D.: Profiles of CH_4, HDO, H_2O, and N_2O with improved lower tropospheric vertical resolution from Aura TES radiances, Atmos. Meas. Tech., 5, 397–411, doi:10.5194/amt-5-397-2012, 2012.

Yoshimura, K., Oki, T., and Ichiyanagi, K.: Evaluation of two-dimensional atmospheric water circulation fields in reanalyses by using precipitation isotopes databases, J. Geophys. Res.-Atmos., 109, D20109, doi:10.1029/2004JD004764, 2004.

Yoshimura, K., Miyoshi, T., and Kanamitsu, M.: Observation system simulation experiments using water vapor isotope information, J. Geophys. Res.-Atmos., 119, 7842–7862, doi:10.1002/2014JD021662, 2014.